2018

APPLICATIONS OF LOW FIELD MAGNETIC RESONANCE IMAGING

Muhammad Waqas
University of the Pacific, waqas_100@hotmail.com

APPLICATIONS OF LOW FIELD MAGNETIC RESONANCE IMAGING

by

Muhammad Waqas

A Thesis Submitted to the

Graduate School

In Partial Fulfillment of the

Requirements for the Degree of

MASTER OF SCIENCE

School of Engineering and Computer Science
Mechanical Engineering

University of the Pacific
Stockton, California

2018

APPLICATIONS OF LOW FIELD MAGNETIC RESONANCE IMAGING

By
Muhammad Waqas

APPROVED BY:

Thesis Advisor: Shadi Othman

Committee Member: HuiHui Xu, Ph.D.

Committee Member: Craig Vierra, Ph.D.

Department Chair: Chi-Wook-Lee

Dean of Graduate School: Thomas H. Naehr, Ph.D

APPLICATIONS OF LOW FIELD MAGNETIC RESONANCE IMAGING

Muhammad Waqas

DEDICATION

This thesis is in dedication to my family for all the sacrifices they have made for my continuing education and for giving me the support every step of the way.

ACKNOWLEDGMENTS

I would like to take this opportunity to thank those that have supported me in various ways. First and foremost, I would like to express my sincerest gratitude to my advisor, Dr. Shadi Othman for his support and guidance through my program. I am grateful to Dr. Othman for sharing his enthusiasm and expertise about MRI and offering me the opportunity to work in the field of elastography. I would also like to humbly thank Dr. HuiHui Xu for her expertise in MRI and passing on to me her knowledge of the subject matter which gave me the tools to confidently conduct my MR experiments; my interest in MRI stemmed from Dr. Xu's class on medical imaging and would like to thank her for instilling in me enthusiasm for the field of MRI. Furthermore, I am very much grateful to Dr. Craig Vierra and would like to thank him for providing his expertise on cell culture work and for allowing me to use the cell culture equipment in his lab to conduct my tissue engineering experiments. His expertise on the subject matter made the cell culturing process simple. I thoroughly enjoyed our insightful conversations while conducting our cell culture work that made the process fun.

Next, I would like to thank Dr. Marcos Gridi-Papp for helping me with the characterization of the resonance frequency of actuators by allowing me to use the Laser Doppler Vibrometer in his lab. The determination of the resonance frequency was crucial for MR Elastography.

Next, I would like to thank Dr. Roshanak Rahimian for allowing me to obtain rat brain samples from her test subjects. This was crucial for the MRE testing process.

Next, I would like to thank Mr. Ernesto Danieli for helping me modify a traditional Spin Echo sequence into one capable of performing elastography. His expertise in the MR software programming prevented potential damage to the MR system.

Finally, I would also like to thank Ms. Delia Davila for her help in designing specialized sample holder for elastography and I would like to thank Mr. Jeremy Hanlon for his expertise in 3-D printing and machining that helped me bring the designs to fruition.

Applications of Low Field Magnetic Resonance Imaging

Abstract

by Muhammad Waqas

University of the Pacific
2018

Magnetic resonance imaging is a non-invasive imaging modality that is used to produce detailed images of soft tissues within the human body. Typically, MRI scanners used in the clinical setting are high field systems because they have a magnetic field strength greater than 1.5 Tesla. The high magnetic field offers the benefit of high spatial resolution and high SNR. However, low filed systems can also produce high resolution MR images with the added benefit of imaging stiffer samples. In this study, a low field 0.5 T MR system was used to image various samples to demonstrate the capability of the low field system in acquiring MR images with resolution comparable to high field systems. Furthermore, the MR system was modified to one capable of performing low field MR Elastography (MRE), a technique that can non-destructively measure the mechanical properties of soft samples. Agarose gel phantom of 0.5% wt. and 1.0% wt. were used to validate the MRE system. Additionally, a rat brain was used to assess the sensitivity of the MRE system in measuring the mechanical properties of small tissues.

The results illustrated that the low field MR system can acquire high resolution images and provide sufficient tissue contrast (e.g through long TE times (80 ms), which is not possible with high field systems). MRE results on gel phantoms illustrated the capability of the low field system to accurately measure the mechanical properties and the MRE testing of rat brain demonstrated the potential of the system to study biological tissues. Finally, the capability of low field MRI and MRE to assess the growth of tissue engineered bone has the potential to transform the field of tissue engineering.

TABLE OF CONTENTS

LIST OF TABLES

LIST OF FIGURES

Introduction

Introduction to MRI

MRI is an imaging modality that is used to produce detailed images of the tissues within the human body. Unlike CT and X-ray, MRI does not rely on radiation, making it a safer imaging technique. The advantages of MRI over other imaging techniques are its noninvasive nature, excellent tissue contrast, and the ability to image in any direction. The technique relies on the fact that tissues have varying magnetic susceptibilities. That is, each tissue has a different degree of magnetization when placed in a magnetic field. This difference serves as a means of identifying the unique tissues within the body based on their contrast in the images. For example, MRI can distinguish between fat and water containing tissues.

The human body is made of mostly water and water is essential for all living cells within the body (Jéquier & Constant, 2010). Water molecules are composed of two hydrogen atoms covalently bonded to one oxygen atom. The hydrogen atom exists in the body in the form of an ion that is commonly referred to as a "proton". Every human cell contains water and therefore contains the protons and these protons have a spin property. This spin property generates a small magnetic field which causes protons to behave like small magnets. Although there are many protons in the body, their random orientations causes their magnetization to cancel out. However, when the patient is placed within a strong magnetic field (B_0), the protons attempt to align either parallel or anti-parallel to

the magnetic field, with a majority favoring alignment in the parallel direction (low energy). This results in the generation of a "net magnetization" that is parallel to the magnetic field (Figure 1). This net magnetization is responsible for the signal that produce MR images.

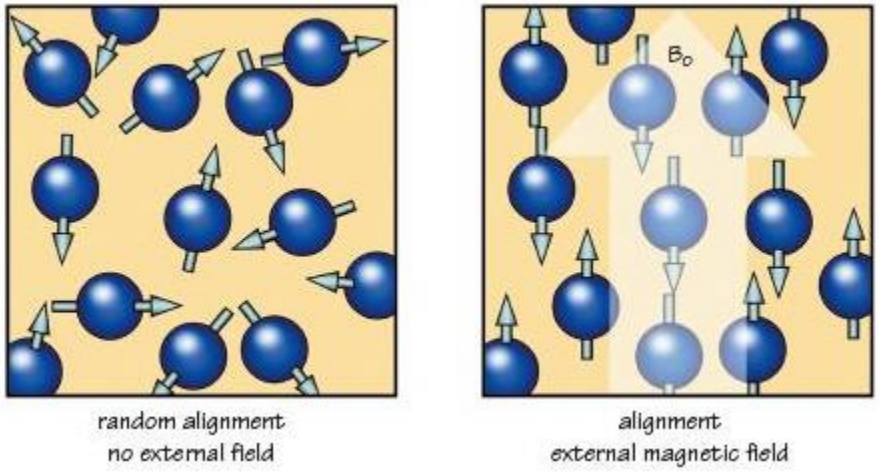

Figure 1: Alignment of protons in a magnetic field. When no external magnetic field is applied, the protons have random alignment which results in zero net magnetization. However, when an external magnetic field (B_0) is applied, the protons align either parallel (lower energy state) or antiparallel (higher energy state) to the magnetic field. Since most protons align parallel to the magnetic field, it results in a net magnetization parallel to the main magnetic field ("MRI at a Glance, 2nd ed," 2012).

In the presence of the magnetic field, the protons attempt to align. However, complete alignment is not achieved due to mechanical forces of the protons' individual components which cause the protons to rotate around in the direction of the magnetic field; this motion is called precession. The frequency at which a proton precesses is found through the Larmor equation which states that the angular frequency is proportional to the magnetic field strength such that

$$\omega = \gamma B_0 \quad (1)$$

The constant γ is the gyromagnetic ratio and is specific to the nuclei used. Table 1 gives the values for the gyromagnetic ratio of several nuclei found in the human body.

Table 1: Values for the gyromagnetic ratio for common ions found in the human tissues. Notice that the ratio is highest for the hydrogen nucleus which is also the most abundant nucleus in the body (Balter, 1987).

Nuclei	**Net spin**	$\frac{\gamma}{2\pi}$ **(MHz/T)**	**Molar concentration (mol/L)**	**Relative sensitivity**
^{1}H	1/2	42.58	99.0	1
^{13}C	1/2	10.71	0.10	0.016
^{14}N	1	3.08	1.6	-
^{19}F	1/2	40.08	0.0066	0.830
^{23}Na	3/2	11.27	0.078	0.093
^{31}P	1/2	17.25	0.35	0.066

Samples placed in a magnet have small atomic dipoles that combine to form a net magnetic moment termed **M**, which grows exponentially. However, since the protons do not precess with the same phase, it is impossible to measure their net magnetization. For measuring their net magnetization, the protons would need to precess with the same phase and the signal would need to be tipped from the direction of the magnetic field into the transverse plane. This can be done by sending a Radio Frequency (RF) pulse that is at the Larmor frequency of the protons, which tips the net magnetization into the

transverse plane and synchronizes the atomic dipoles. Once the atomic dipoles are synchronized, the RF pulse is removed. When the RF pulse is removed, the protons return to their relaxed state (relaxation) by releasing energy which is used to produce an image. The relaxation process for hydrogen protons occurs by two main mechanisms: spin-lattice (T_1) relaxation and spin-spin (T_2) relaxation. Variations in these two mechanism gives contrast to MR images.

Relaxation Times. At equilibrium, the net magnetization vector lies along the direction of the applied magnetic field (B_0) and is termed the equilibrium magnetization (M_0). In this configuration, there is no transverse magnetization (M_X and M_Y) and the net magnetization, M_Z, is equal to equilibrium magnetization M_0. It is possible to change the net magnetization vector by applying energy of a specific frequency, a 90° RF pulse for example, to the nuclear spin system. If enough energy is applied, then the longitudinal magnetization can be decreased to zero. As the magnetization returns to equilibrium, the longitudinal magnetization grows according to

$$M_z(t) = M_0\left(1 - e^{-\frac{t}{T_1}}\right). \quad (2)$$

The time constant that describes how the longitudinal magnetization returns to its equilibrium value is the longitudinal or spin-lattice relaxation time (T_1). The longitudinal relaxation time can be viewed as the time required for the longitudinal magnetization (M_Z) to reach 63% of its maximum value (

Figure **2**). This occurs due to the transfer of energy between neighboring spins as they move at random and their environment as collisions occur. The T_1 relaxation time

varies between different tissues which allows for specialized sequences to produce contrast between the images (T_1-weighted images).

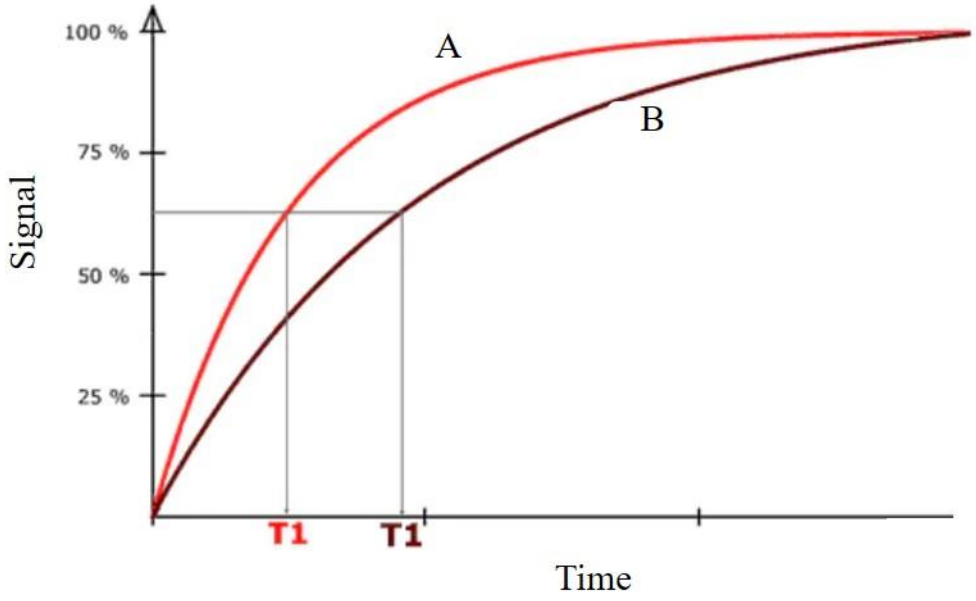

Figure 2: Recovery of the longitudinal magnetization for two different tissues. Tissue A has a shorter T_1 relaxation time than Tissue B which gives contrast between the two tissues.

Another important relaxation parameter is the spin-spin relaxation time, T_2. After the 90° RF pulse, the net magnetization tips by 90° and lies in the transverse plane. This net magnetization is composed of the contributions from numerous protons which precess at the Larmor frequency. When the 90 RF pulse is applied, the protons are in phase and remain in phase immediately after the RF pulse. However, do the interactions of local nuclei (spin-spin interactions), the magnetic field in the immediate environment of a proton is not homogeneous. This means that each nucleus has a slightly different Larmor frequency, which causes the dephasing of the transverse magnetization. The degree of

dephasing is dependent on the elapsed time; with a longer elapsed time corresponding to greater phase difference. This makes the transverse magnetization decay exponentially according to

$$M_{xy}(t) = M_{xy}e^{-\frac{t}{T_2}}. \quad (3)$$

In addition to the dephasing caused by spin-spin interactions, the decay of the transverse magnetization is also affected by the small inhomogeneities in the magnetic field (B_0), chemical shift, and magnetic susceptibility that is termed T_2'. Therefore, the signal decays faster than it would for pure T_2 (

Figure **3**). The cumulative effect of this phenomenon is termed T_2 * and is given by the equation,

$$\frac{1}{T_2^*} = \frac{1}{T_2} + \frac{1}{T_2'}. \quad (4)$$

Like T_1, T_2 relaxation time varies between tissues and can serve as a means for finding contrast between MR images.

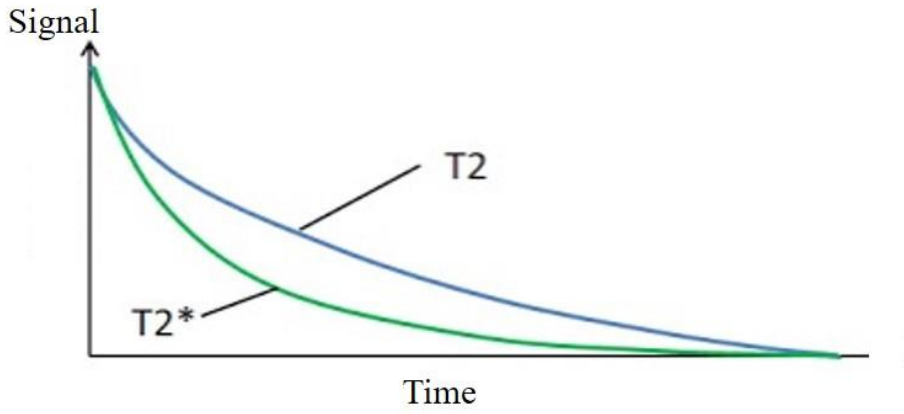

Figure 3: Comparison of signal decay for pure T_2 and T_2^*. Due to inhomogeneities in the main magnetic field, chemical shift, and magnetic susceptibility, the spin-spin relaxation decays at a faster rate.

Although T_1 and T_2 relaxation times are discussed separately, they in fact occur simultaneously. The dephasing of the transverse magnetization leads to its decay (governed by T_2) but results in the growth of the longitudinal magnetization (governed by T_1).

Imaging Sequences. As discussed, after the 90° RF pulse, the net magnetization begins to dephase in the transverse plane. However, after a certain amount of time, a 180° RF pulse can be applied that causes the spins to rotate over to the opposite axis and results in the rephasing of the net magnetization. The rephrasing of the spins forms an "echo" termed a spin echo and the time between the 90° RF pulse and the peak of this echo is called the echo time (TE). TE along with several other parameters can be used to control the timing of the RF pulse and the magnetic field gradients which ultimately helps to achieve contrast in the image. These parameters are grouped into what is known as an imaging sequence. A typical spin echo imaging sequence is illustrated in

Figure ***4***. In the sequence, three gradients, frequency encoding (G_X), phase encoding (G_Y), and slice select (G_Z) are used to perform spatial localization of protons.

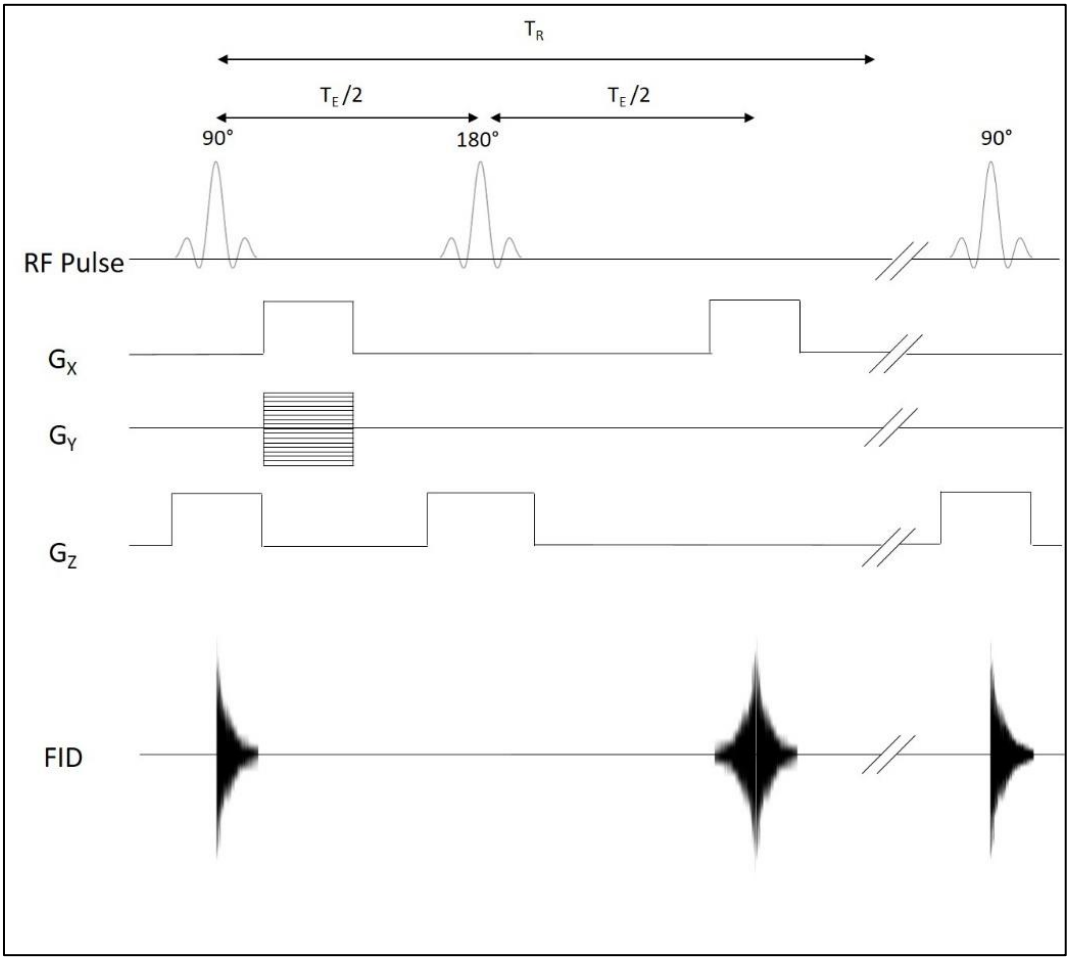

Figure 4: Typical spin echo imaging sequence. The repetition time (TR) is shown as the time it takes to go through the sequence once. The time of the echo is shown as TE. This sequence uses a 90° RF pulse followed by a 180° RF pulse to rephrase the spins and form an echo.

The TE and the repetition time (TR) can be adjusted to control for the weight of the T_1 and T_2 effects in the image. Table 2 presents relaxation values of varying tissues that comprise the human brain obtained at a magnetic field of 1 T. While T_1 and T_2 values depend on the nuclear properties of the proton, proton density weighted imaging makes use of the relative density of the protons in the tissues; this gives the technique features of the both T_1 and T_2 relaxation times.

Table 2: Typical values for T_1 and T_2 relaxation times for various tissues within the human body obtained at a magnetic field strength of 1 T (Prince & Links, 2006).

	T₁ **(ms)**	***T₂*** **(ms)**	**Proton**
White matter	510	67	0.61
Gray matter	760	77	0.69
Cerebrospinal Fluid	2650	280	1.00

Using the differences between these components, contrast can be produced in the image. For a T_1 weighted image, a short TR is selected to optimize the T_1 contrast and a short TE is selected to minimize the influence of T_2 and maximize the intensity of the signal. For T_2 weighted images, a long TR and a long TE are used but a long TE implies a reduction in the signal intensity and therefore a reduction in the single to noise ratio. For the proton density weighted imaging, a long TR and a short TE are used which minimizes the effects of T_1 and T_2 while maximizing the signal. Figure 5 lists examples of images obtained through these three differing contrast mechanisms. It is however, important to note that aside from these, other contrast mechanisms do exist; for example magnetic resonance elastography (MRE).

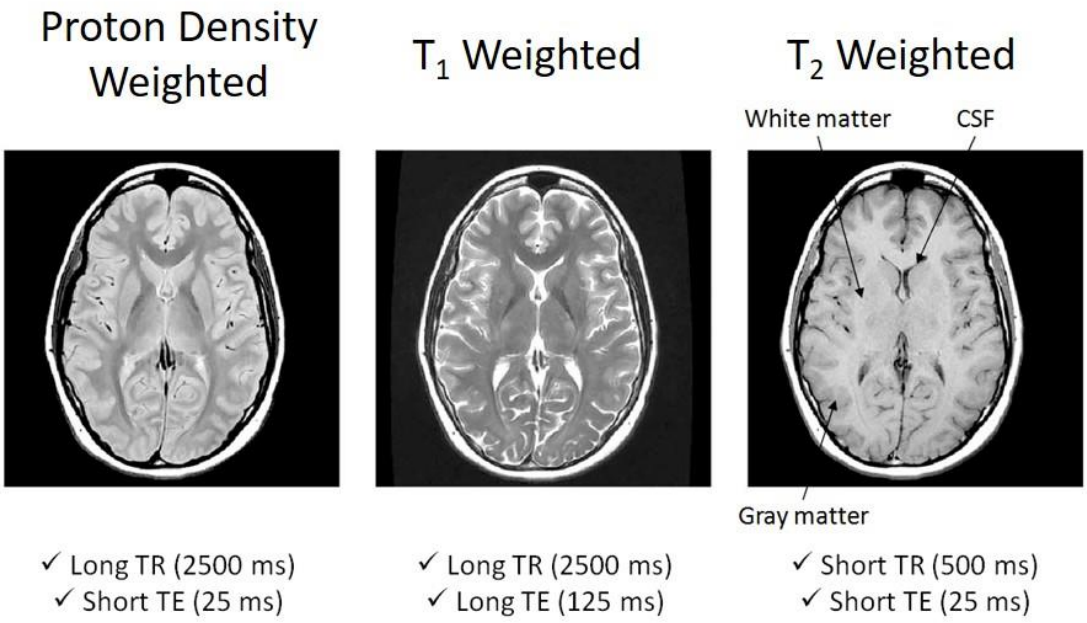

Figure 5: Images of the bran obtained with the different contrast mechanisms: proton density weighted, T_2 weighted, and T_1 weighted obtained at a field strength of 1 T (Prince & Links, 2006).

Introduction to MRE

A major goal of medicine is to measure the integrity of tissues without invasive procedures. Current methods of detecting cancerous or diseased tissue involves rudimentary techniques such as palpation or extensive lab tests and biopsies. Tissue is extracted from the patient and analyzed under a microscope for signs of tumor growth, and therefore, the patient needs to undergo surgery for the tissue extraction. This results in patient discomfort and higher medical costs. Palpation is a clinical examination tool that has been used for centuries to detect abnormalities in parts of the human body that are easily accessible by assessing the changes in the stiffness of tissues (R. Muthupillai et al., 1995). The elasticity of tissues in the human body is well known and therefore, a

change in elasticity may indicate the presence of disease (Doyley & Parker, 2014). Recent advancement of medical technology has allowed use of imaging techniques for analyzing the tissues within the human body. X-ray imaging has come to be a significant means of detecting bone damage; CT imaging has allowed for the volumetric imaging of various areas of the body; and MRI has provided enhanced soft-tissue contrast with no harmful radiation. However, these techniques fail to quantify the changes in the mechanical properties of the tissues due to disease. Mechanical properties like the shear modulus of tissues vary more than 5 orders of magnitude while other tissue properties assessed by traditional imaging modalities vary much less (Figure 6). This gives the measurement of the shear wave modulus significant diagnostic potential. For example, palpation is one method used for testing the relative hardness of tumors in cases of breast cancer (Hawley et al., 2017). However, palpation is subjective and limited to areas of the body that are easily accessible. Therefore, new technologies are needed to address the limitations of palpation while non-destructively providing quantitative information about tissue properties. MRE is a technique that can be used to determine the mechanical properties of samples by analyzing the visual and temporal strains caused by the propagation of mechanical shear waves (Raja Muthupillai & Ehman, 1996).

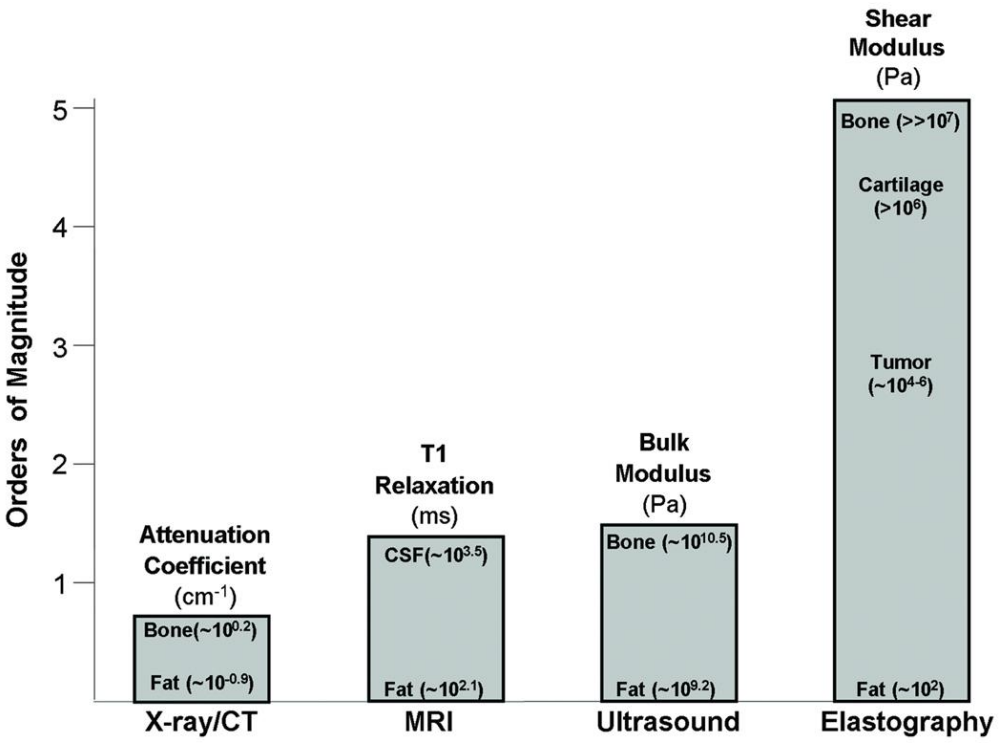

Figure 6: Example of different imaging modalities and the contrast spectrum they use. The shear modulus shows the largest variation with a range of values that span over 5 orders of magnitude (Faruk, Islam, Arefin, & Haq, 2015; Mariappan, Glaser, & Ehman, 2010).

MRE Principles. MRE has become a useful tool in investigating various diseases within the body based on the mechanical properties of diseased tissues. There are three main steps involved in MRE:

i. Producing cyclic shear motion in the sample via a mechanical actuator.

ii. Using a modified pulse sequence that contains motion-sensitizing gradients (MSG) to monitor shear wave motion through the sample.

iii. Using an inversion algorithm to evaluate the local values of the mechanical properties.

The mechanical waves used in MRE are typically of a single frequency and are generated by an external waveform generator. The electronic signal is triggered by the modified pulse sequence and fed into a signal amplifier before stimulating a mechanical actuator. The following section will discuss the theoretical basis of MRE.

Theoretical Basis of MRE. MRE is a phase-contrast MRI technique that measures the displacement of spins subjected to cyclic mechanical excitations (R. Muthupillai et al., 1995). Typically, in MR acquisition, the phase image is not useful because it is contaminated by system imperfections such as magnetic susceptibility (Brown, Haacke, Cheng, Thompson, & Venkatesan, 2014). However, useful data can be obtained if the phase images are represented as phase difference images, which plot the difference between the phases of two data sets. Assuming images A and B, this could be represented as

$$\phi(x,y) = \phi_A(x,y) - \phi_B(x,y)\,. \tag{5}$$

This phase difference is typically used to correct for system imperfections and MR nuances. However, the information provided by the phase difference can be used to generate contrast related to motion by intentionally introducing controlled motion artifacts into a phase image and studying these phenomena related to motion by magnetic field gradient sensitization. Since the spins in a magnetic field possess a phase that is dependent on the strength of the magnetic field and the applied magnetic field along the direction of the spin motion, the phase equation is correlated to spin motion by

$$\phi = \gamma \int_0^\tau \overrightarrow{B_0} \cdot \vec{r}(t)dt + \gamma \int_0^\tau \overrightarrow{G_E} \cdot \vec{r}(t)dt + \gamma \int_0^\tau \overrightarrow{G_r}(t) \cdot \vec{r}(t)dt\,, \tag{6}$$

where γ is the gyromagnetic ratio characteristic of the nuclei, $\overrightarrow{B_0}$ is the static magnetic field strength, $\overrightarrow{G_E}(t)$ is one of the encoding gradient vectors, $\vec{r}(t)$ is the spin motion vector, and $\overrightarrow{G_r}(t)$ is the bipolar gradient vector that is collinear to the encoding gradient and used for spin motion filtering. This gradient is also known as the motion sensitizing gradient (MSG) (Brown et al., 2014).

When the difference between the phase images is taken, the phase due to the encoding gradient and the static magnetic field is assumed to be constant through the bipolar measurements and can be eliminated by the subtraction. However, the motion induced by the bipolar gradients can be reversed which makes it doubled. Consequently, only the third term of equation (6) remains and is used for motion detection, so that

$$\phi = \gamma \int_0^{\tau} \overrightarrow{G_r}(t) \cdot \vec{r}(t) dt \tag{7}$$

A cyclic induced displacement will cause a temporal spin motion vector governed by

$$\vec{r}(t) = \overrightarrow{r_0} + \vec{\xi}(\vec{r}, t), \tag{8}$$

where $\overrightarrow{r_0}$ represents the initial location of the spin at time t = 0, and $\vec{\xi}(\vec{r}, t)$ is the cyclic displacement of the spin about its mean position caused by the mechanical excitation. If the MSG, with multiple bipolar pairs *N* and duration τ, is synchronized at the same frequency with the induced spin motion, $\vec{\xi}(\vec{r}, t)$, and turned on for a duration τ so that $\int_0^{\tau} \overrightarrow{G_r}(t) \cdot \overrightarrow{r_0} dt = 0$, then the dynamic phase shift of the moving magnetization, equation (7), can be rewritten as

$$\phi = \gamma \int_0^{\tau} \overrightarrow{G_r}(t) \cdot \vec{\xi}(\vec{r}, t) dt \tag{9}$$

The cyclic displacement vector $\vec{\xi}(\vec{r}, t)$ can be further written as

$$\vec{\xi}(\vec{r}, t) = \overrightarrow{\xi_0}\, e^{(j[\vec{k}\cdot\vec{r} - \omega t + \psi])} \tag{10}$$

where $\overrightarrow{\xi_o}$ is the peak displacement of the spin from the mean position, $\vec{k}$ is the wave vector, ω is the angular frequency of the mechanical wave excitation, and ψ is the introduced phase offset between the bipolar gradient pulses and the wave.

The phase difference depends on the shape of the bipolar gradient and typically, the biopolar gradient is set to be a sinusoidal, $\overrightarrow{G_r}(t) = \overrightarrow{G_0}\, cos(\omega t)$, which reduces equation (10) to a phase constant that is a function of position and phase shift given by

$$\begin{aligned} \phi(\vec{r}, \psi) &= \gamma \int_0^{\tau} \overrightarrow{G_0} \cos(\omega t) \cdot \overrightarrow{\xi_0}\, e^{(j[\vec{k}\cdot\vec{r} - \omega t + \psi])} dt \\ &= \frac{\gamma N T \left(\overrightarrow{G_0} \cdot \overrightarrow{\xi_0}\right)}{2} \cos\left(\vec{k} \cdot \vec{r} + \psi\right) \end{aligned} \tag{11}$$

where the MSG duration is written as $\tau = NT$, N being the number of bipolar pairs and $T = 2\pi/\omega$. Equation (11) shows that the measured phase magnitude is dependent on the number of bipolar pairs N, the dot product of the amplitude of the bipolar gradient and the peak displacement spin amplitude motion ($\overrightarrow{G_0} \cdot \overrightarrow{\xi_0}$) modulated by the cosine function. From the dot product relationship, it is determined that the bipolar gradient acts as a filter extracting its collinear displacement. Furthermore, there is a relation between the measured phase shift and the initial phase offset ψ so by varying ψ, it is possible to study the temporal behavior of spin displacements.

A typical spin-echo based MRE pulse sequence is shown in

Figure *7*, with the RF pulse waveform, slice-selection (G_Z), phase-encoding gradient (G_Y), and the frequency-encoding gradient (G_X).

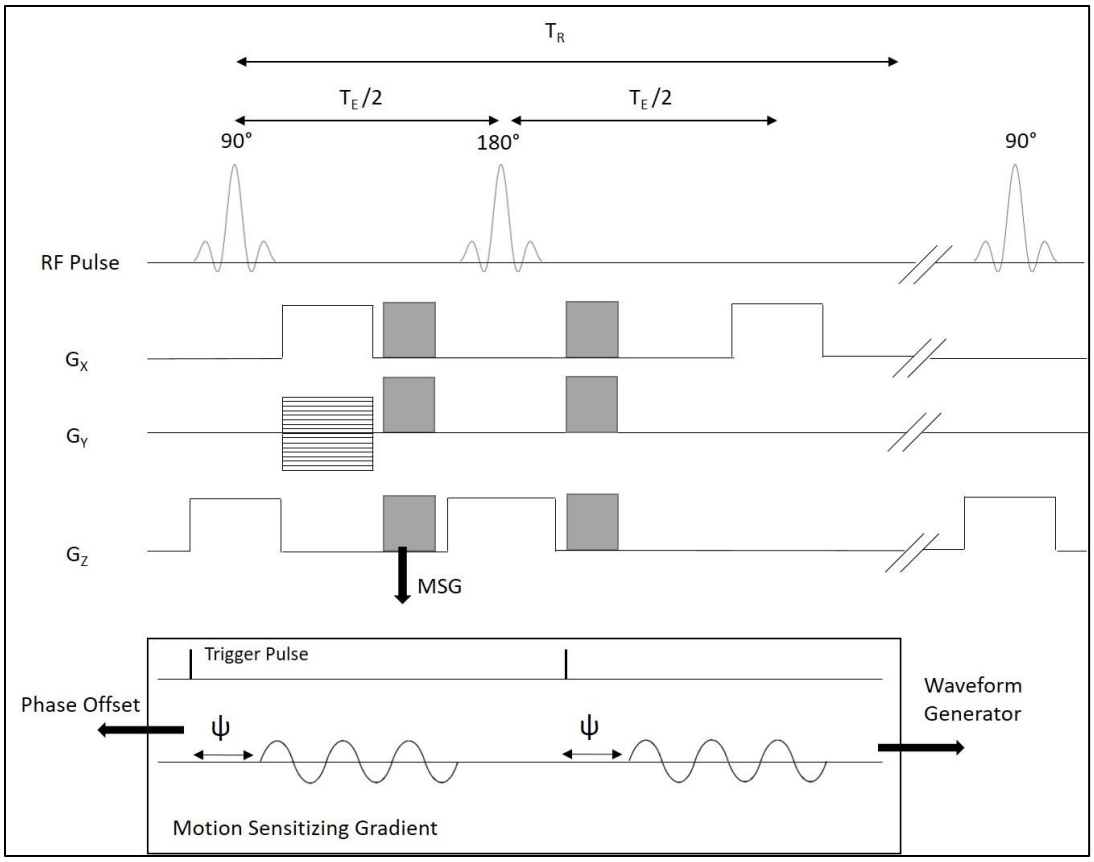

Figure 7: A typical MRE spin-echo sequence. The motion sensitizing gradient (MSG) is shown with a positive sinusoid. ψ is the delay between the motion waveform and the MSG. Adapted from (Boulet, Kelso, & Othman, 2011).

By manipulating the axis on which the MSGs are applied, the motion occurring in any direction can be encoded in the phase of an MR image. Two phase images are

collected, one with a positive MSG and the other with a negative MSG, and a phase-difference image is calculated by subtraction or complex division, removing all phase information not related to the imparted motion. The phase offsets ψ are evenly distributed over a period of the mechanical excitations to acquire time-dependent data showing the propagation of the wave through the tissue of interest. The motion-encoding capability of this technique is sensitive enough to detect motion on the order of 100 nanometers (Raja Muthupillai & Ehman, 1996).

The data obtained from a complete MRE acquisition in a single plane is composed of several images that are evenly distributed over one cycle of the mechanical excitations. These images are grouped into a three-dimensional dataset (2 spatial and 1 temporal dimensions) depicting shear wave propagation. Each image typically contains 128 x 128 pixels whose intensity corresponds to the magnitude of the measured displacement in the direction of the motion sensitizing gradient. The last step in MRE is to calculate local values of mechanical properties from this measured displacement field. This can be done by performing a direct algebraic inversion of the governing equations under certain simplifying assumptions, details of which are explained in (Boulet et al., 2011).

MRE Applications

Due to its noninvasive nature, MRE has found many applications and has transformed medical imaging. MRE has been used to test various organs within the body including liver, kidney, brain, breast, and bone (Kruse et al., 2008; Shah et al., 2004; L. Xu, Lin, Xi, Shen, & Gao, 2007; Yin et al., 2007).

One of the main applications of MRE in the clinical setting is the diagnosis of liver disease (Rouvière et al., 2006; Yin et al., 2007). Severe damage to the liver can result in the tissue fibrosis (scarring of the tissue) which can further advance to irreversible cirrhosis (diseased liver tissue). MRE is used to assess the disease researchers have demonstrated that fibrosis causes an increase in the liver tissue stiffness (Batheja et al., 2015; Besa et al., 2017). Furthermore, MRE has been shown to be sensitive enough to assess the progression of fibrosis, with a cutoff stiffness of 2.93 kilopascals (kPa) signifying onset of the disease, as shown in Figure 8. Other noninvasive modalities like conventional MRI, CT, and US are able to detect advanced cirrhosis but have low sensitivity for the, early, fibrotic stages of the disease, which limits treatment options (Faria et al., 2009).

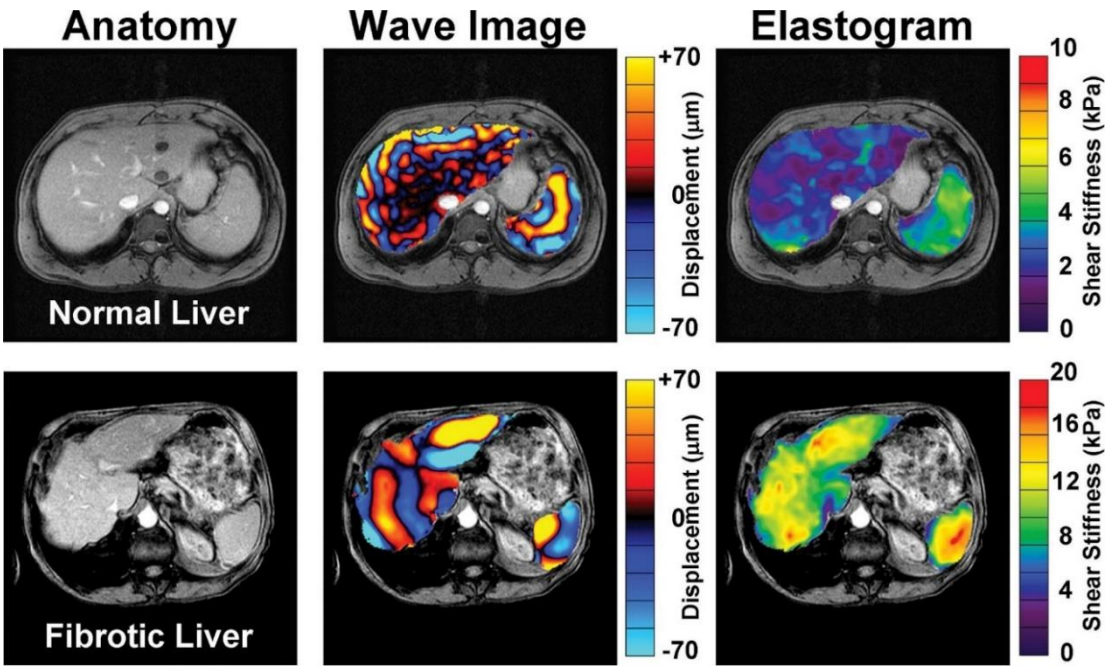

Figure 8: MRE of a healthy liver and a diseased liver. The left column shows anatomic images of a healthy liver as compared to a liver with grade 4 fibrosis. The middle column shows the shear wave data of the liver and spleen superimposed on the anatomical images. The far right column shows the elastograms. The shear wave images show an increased wavelength in the fibrotic liver. The elastograms show an increased mean shear stiffness in the fibrotic liver as compared to the normal liver. (12.1 ± 1.2 kPa vs 1.8 ± 0.3 kPa, respectively) (Yin et al., 2007).

Investigation of the brain requires noninvasive procedures since the brain is encased in the skull. While conventional MRI or CT can be used for the detection of brain injury or disease, they provide limited information. MRE, however, is well suited for this application. MRE has shown promise in studying the effects of traumatic brain injury (TBI) and can be used to diagnose neurodegenerative disorders (Boulet et al., 2011; Lipp et al., 2018; Murphy et al., 2016). TBI causes significant compression of the brain tissue which triggers specific biological responses (edema, death of neuronal cells, and activation of glial cells), that can change the elasticity of the tissue which is

measurable by MRE. Conventional MRI can give detailed images of the injured site but does not provide quantitative information on the extent of the injury.

Efforts have been made to assess brain tissue mechanical properties with MRE with the goal of using the technique as a potential diagnostic tool for studying neurodegenerative diseases like Alzheimer's disease (AD). AD is a major neurodegenerative disorder that is characterized by the progressive impairment of cognitive function. The impairment of the cognitive function occurs due to the degeneration of the nerve fibers in the brain, which effect the frontal, parietal, and temporal lobes. MRE has been used to detect changes in stiffness in the frontal, parietal, and temporal lobes which correlates with the known pathology of the disease. (Murphy et al., 2016)

A significant application MRI and MRE is to study the development of engineered tissues. It is essential to that engineered tissues possess mechanical properties like the natural tissues they are meant to replace. The growth of tissue engineered cartilage has been studied using MRE in an ectopic mouse model. Human Mesenchymal Stem cells were differentiated on silk, collagen and gelatin scaffolds and implanted subcutaneously in mice and imaged at 9.4 T (Khalilzad-Sharghi, Han, Xu, & Othman, 2016). As shown in Figure 9, MRE characterized the development of the cartilage tissue and provided a quantitate measure of the growth. The findings of this study were significant because it demonstrated the capability of assessing tissue engineered construct growth in an *in vivo* mouse model.

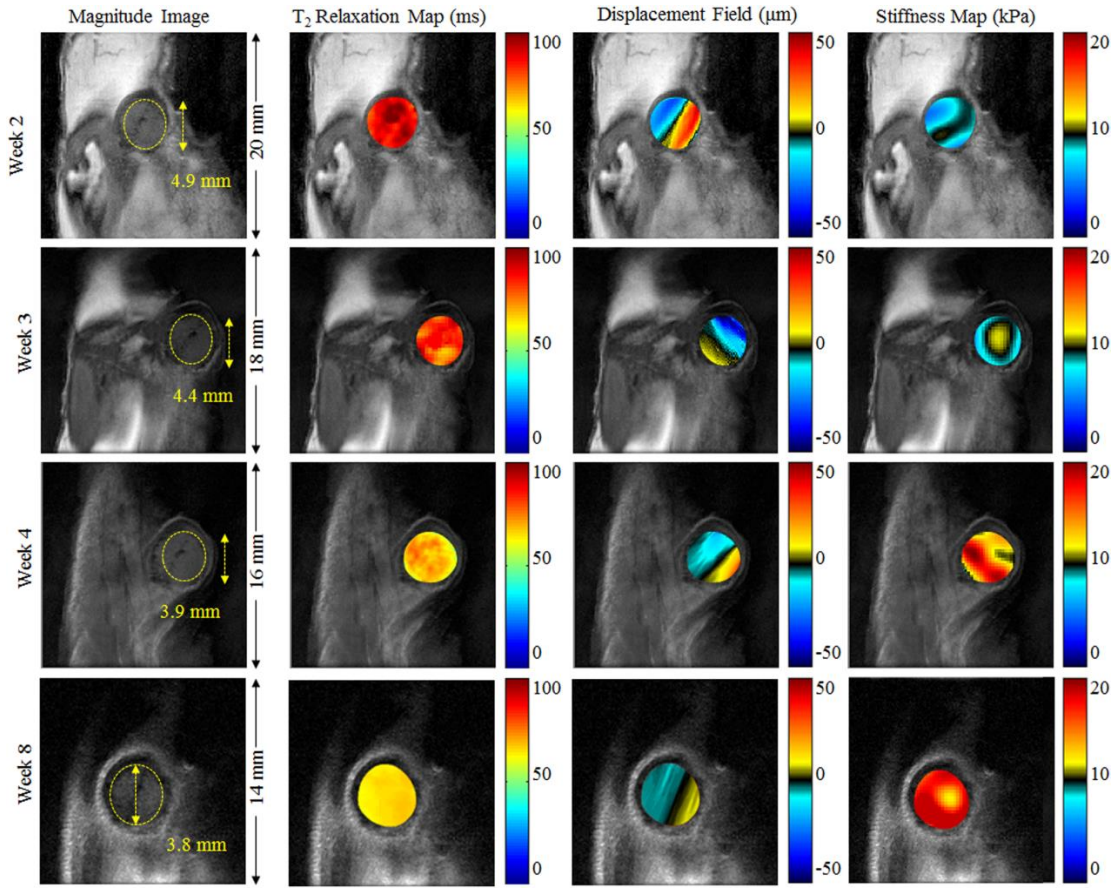

Figure 9: Tissue engineered cartilage evaluated over an 8-week study. From left to right, a magnitude image obtained through a spin echo sequence, T_2 relaxation maps, displacement fields, and stiffness maps of the constructs. The figure shows the capability of MRI and MRE conducted at 9.4 T to assess the growth of engineered tissues in an in vivo model (Khalilzad-Sharghi et al., 2016).

Thesis Objective

The objective of this study is to show the ability of low field MRI to acquire images with high spatial resolution and show its potential use in determining the mechanical properties of samples through MRE.

Methods

MR Imaging System

MR images were acquired on a novel, table-top low field MR imaging system as shown in Figure 10. Image acquisition conducted at 21 MHz in a 45-cm vertical bore magnet (Magritek, Aachen, Germany) with a magnetic strength of 0.5 T, a five-cm RF solenoid coil with triple axis gradients (maximum strength of 0.25T/m) giving maximum isotropic resolution of 200 micrometers.

MR Imaging Procedure

MR images were acquired for a variety of different samples such as fruit and tissue samples. The samples were limited by the dimensions of the sample holder, shown in Figure 10b. The MR acquisitions were performed with typical parameters such as, TR of 1 s, TE of 10 – 80 ms, and number of averages (NEX) of 2-128. The field of view (FOV) was adjusted based on the sample geometry and the desired sample resolution. Solid samples were typically saran wrapped prior to placement in the holder. This facilitated holder cleaning process. Samples that required liquid medium were simply placed in the holder with the required medium; afterwards the holder was cleaned thoroughly to prevent contamination of other samples.

Figure 10: a) Table top low field MRI system used in this study. b) Sample holder and maximum sample dimensions.

MRE System Setup

MR Sequence Modification. For MRE experiments, a traditional spin echo sequence was modified to include the MSG gradient frequency, number, and strength. The native system imaging software PROSPA (Magritek, Aachen, Germany) gave the user the ability to set the MRE parameters. The spin echo sequence used in MRE experiments is illustrated in

Figure 7. The choice of gradient for the pulse sequence was a sinusoidal pulse because the inversion algorithm used specified the use of sinusoidal waveform. The MSG gradient was placed along the phase encoding gradient.

Actuator Characterization. For all experiments, a piezoelectric bending actuator (Piezo systems, inc., Woburn, MA) provided the displacement for the system and was synchronized with the spin echo pulse sequence. The actuator was driven by signal produced by waveform generator (DG1000Z, Rigol, Beaverton, OR) and amplified by a linear amplifier (EPA-104-115, Piezo systems, inc., Woburn, MA). The actuator was coupled with the sample via a thin needle approximately the size of an electronic pin that was soldered onto the non-fixed end of the actuator.

To ensure the optimal performance, a Laser Doppler Vibrometer was used to characterize the actuator under loading conditions (Figure 11). When a laser beam is projected on the surface of the actuator, the reflected signal indicates the actuator's displacement. This allows for the determination of the actuator's resonance frequency, the frequency that produces the greatest displacement. The resonance frequency can be found by driving the actuator at 20 V_{PP} with band limited noise input sweeping from 0.02 – 1 kHz in 10 ms cycles. Once the resonance frequency was found, the waveform generator was used to drive the actuator at that frequency to determine the displacement. Once it was verified, that the specific frequency produced the greatest displacement, that frequency was selected for the MRE experiment. Depending on the loading condition, the resonance frequency was found to be 370-420 Hz with a displacement of 145 – 200 microns.

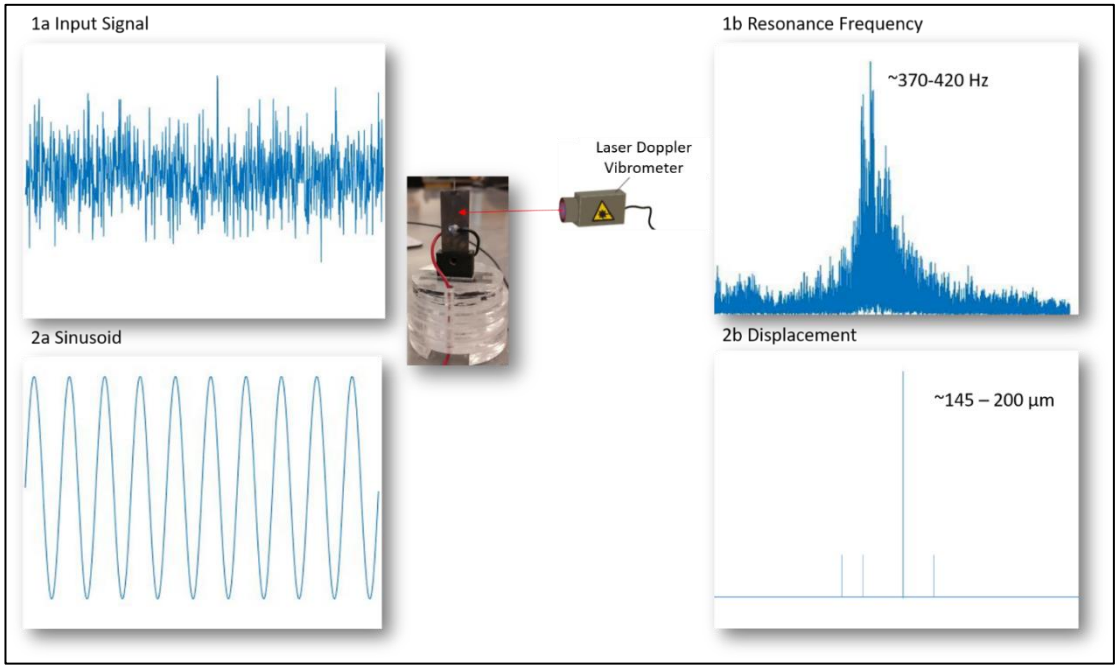

Figure 11: Setup to characterize the resonance frequency of the actuator. 1a) Band-limited white noise was input into the actuator. 1b) The actuator response was measured and the frequency that produced the greatest displacement was determined. 2a) A sinusoidal wave at the resonance frequency was input to the actuator. 2b) The maximum displacement with the sinusoidal wave was determined.

MRE Experimental Setup

First MRE was tested with a gel phantom of 0.50% wt. concentration. The gel was made by mixing 0.5 g of agarose gel (SeaKem, Lonza, Rockland, ME) in 100 ml of deionized water and heating it in a microwave oven on high power for 2.5 minutes. The gel was placed in the sample holder and allowed to cool to room temperature. MRE acquisition of the 0.50% wt. gel phantom was executed with the following parameters: TR of 2 ms, TE of 30-60 ms, slice thickness of 10 mm, a FOV of 90 x 90 mm, and with 8 MSG at a frequency of 300 Hz.

Second, MRE was tested with a sample made from two gels of different concentrations. The top layer was made with a concentration of 0.5% wt. and the bottom layer was made with a concentration of 1.0% wt. The gel phantom was tested with the modified spin echo sequence with the following parameters: TR of 2 s, TE of 30 ms, slice thickness of 10 mm, a FOV of 90 x 90 mm, and with 8 MSG at a frequency of 400 Hz. The sequence was run with a MSG offset ranging from 0 to 2π at an interval of $\frac{1}{8}\pi$. Upon the collection of the motion encoded images, the files were loaded into Matlab 2016 and complex division was used to produce the phase difference images. These images were saved as Matlab data files and imported into the inversion algorithm developed by Thomas Boulet. This algorithm uses the three-dimensional dataset (two spatial, 1 temporal) to derive the shear wave speed, wave attenuation, shear stiffness, shear elasticity, shear viscosity, etc.

Third, MRE was tested with a rat brain sample. The brain was placed on top of an agarose gel of 1.0% concentration and surrounded by agarose gel of 0.25% wt. concentration. The test was performed with the following parameters: TR of 4 s, TE of 60 ms, slice thickness of 10 mm, FOV of 90 x 90 mm, and 8 MSG with a frequency of 400 Hz.

Results

MRI Testing

High Resolution Images

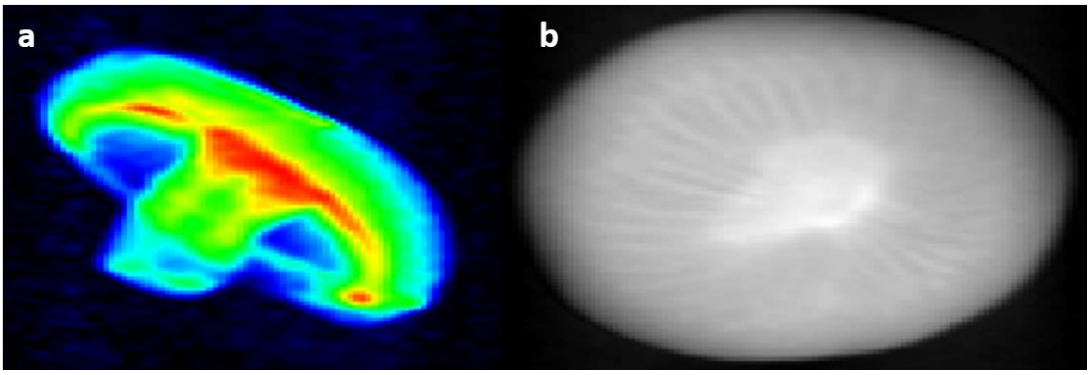

Figure 12: a) Sagittal MR image of a mushroom showing high spatial resolution is possible with a low field system. Image taken with a spin echo sequence with an in-plane resolution of 0.703 mm, 40 mm slice thickness, TR of 1 s, TE of 5 ms, and NEX of 1. b) Axial MR slice of a kiwi showing high spatial resolution and ability of MRI to show internal structure of the fruit. Image in-plane resolution of 0.703 mm, 10 mm slice thickness, TR of 1 s, TE of 5 ms, and NEX of 1.

Ex Vivo Brain Imaging: Effect of Increased Number of Averages

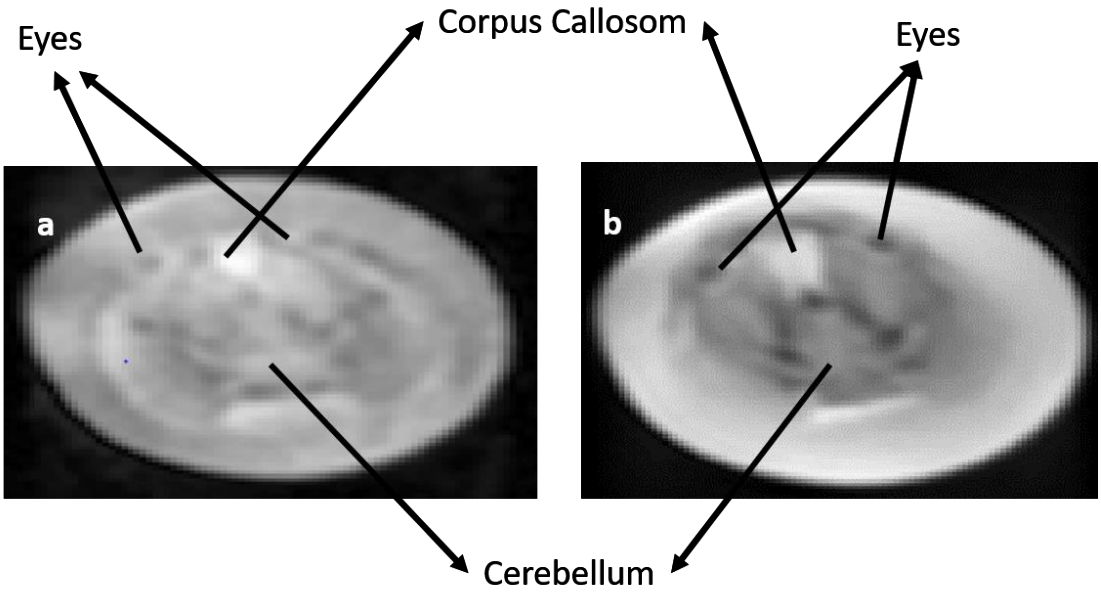

Figure 13: Transverse MR images of an ex vivo rat brain in formalin taken with a spin echo sequence with a TR of 4 s, TE of 45 ms, slice thickness of 10 mm and in plane resolution of 0.390 mm. a) Image taken with 16 averages. b) Image taken with 256 averages. These images show an increase in number of averages leads to an increase in resolution of the image.

Ex Vivo Brain Imaging: T2 effect

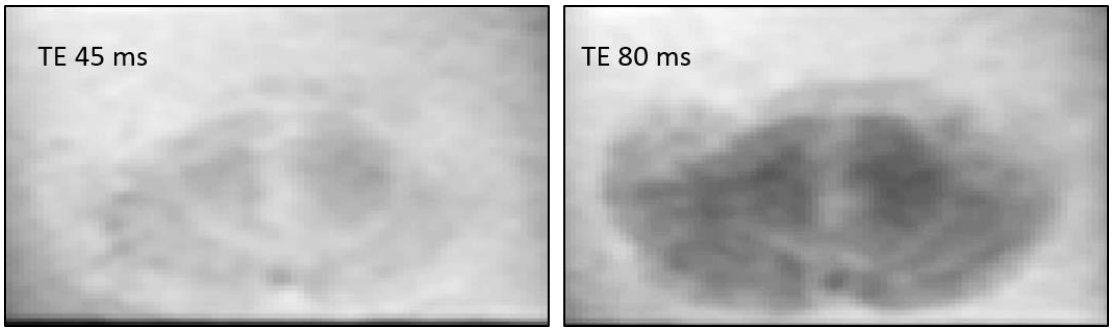

Figure 14: MR images of the brain taken with two different echo times (TE) to show the effect of T_2 on the image. The image obtained with a higher echotime of 80 ms shows more spatial detail of the brain than the image with the lower echotime. Image taken with a spin echo sequence with an in-plane resolution of 0.195 mm, 10 mm slice thickness, TR of 4 s, and NEX of 512.

MRE Validation

Agarose gel of 0.50% wt. Concentration. MRE was validated through two gel phantom experiments. In the first experiment, a gel phantom of 0.50% wt. was used to determine if indeed, the MRE can successfully be implemented with a low field system.

Figure 15 shows the resulting magnitude and shear wave images and the vertical line profile through the sample. The phase difference image shows the propagation of the shear waves through the sample. The line profile shows the sinusoidal wave through the sample and gives the wavelength. The wavelength for the wave was found to be approximately 7 mm.

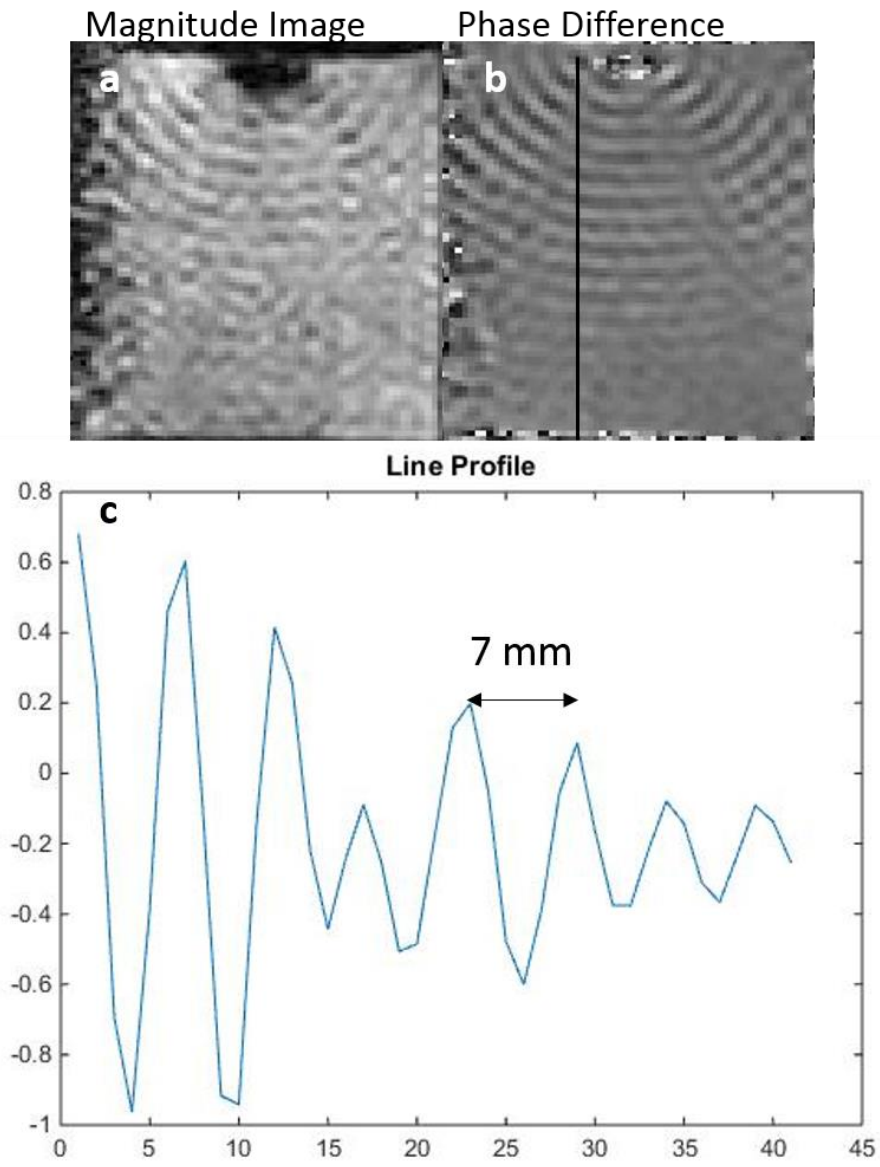

Figure 15: MRE validation through a 0.50% wt. gel phantom test. The image is taken with a spin echo based MRE sequence with an in-plane resolution of 0.703 mm, a slice thickness of 10 mm, TR of 2 s, TE of 30 ms, NEX of 1, with 8 MSG at a frequency of 300 Hz. a) Magnitude image of gel phantom with sufficient resolution. b) Phase difference image showing the shear wave through the sample. c) A vertical line profile through the sample illustrating the sinusoidal wave and showing that the wavelength is approximately 7 mm.

Two Layered Agarose Gel. Following the testing of a sample consisting of a gel of 0.5% wt. stiffness, MRE was tested with a sample containing gels of two stiffnesses (0.50% and 1.0% by wt.). Figure 16 shows the resulting phase difference map, line profile, and the stiffness map. The phase difference image shows that as the waves travel from the less stiff gel of 0.5% wt. to the stiffer 1.0% wt. gel, the wavelength changes. This is evident in the line profile, where the waves through the 0.5% wt. gel had a wavelength of 7 mm whereas the wavelength increased to 14 mm in the stiffer gel. The stiffness map provides both quantitative and qualitative information of the stiffness. The stiffness is approximately 25 kPa for the 1.0% wt. gel and 10 kPa for the 0.50% wt. gel.

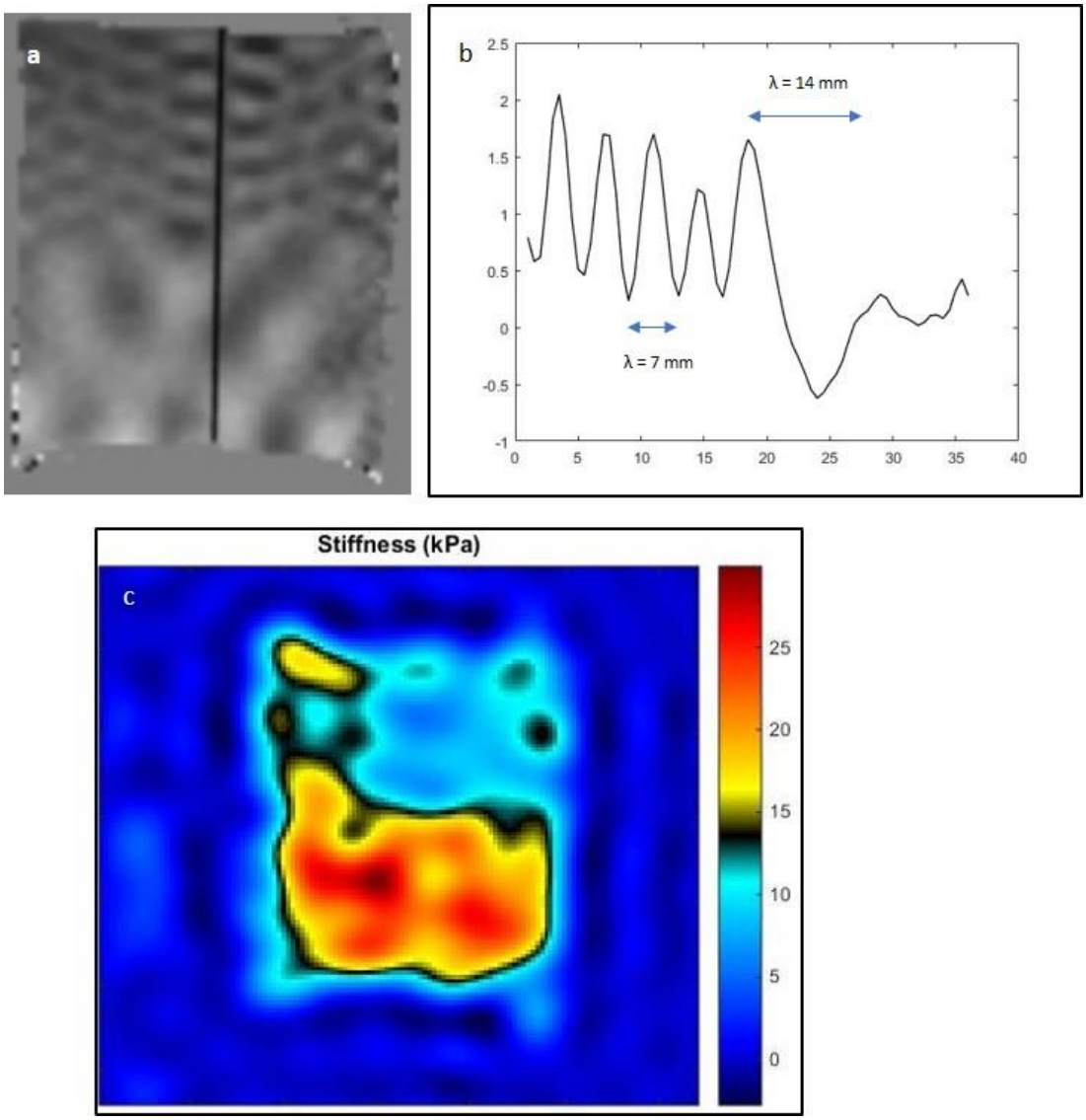

Figure 16: MRE performed on a gel phantom consisting of gels of two different stiffnesses (0.50 % on top and 1.0 % on bottom). The image is taken with a spin echo based MRE sequence with an in-plane resolution of 0.703 mm, a slice thickness of 10 mm, NEX of 2, TR of 2 s, TE of 30 ms, and with 8 MSG at a frequency of 400 Hz. a) Phase difference image showing the shear wave through the gel phantom of two stiffnesses. b) A vertical line profile through the sample illustrating the sinusoidal wave and showing the change in wavelength as the wave travels from the less stiff (0.5% wt.) to the stiffer (1.0% wt.) gel. c) A stiffness map showing the stiffness of the sample on a pixel-by-pixel basis. The map approximates the stiffness of the 0.5% wt. gel to be 10 kPa and the stiffness of the 1.0% wt. gel to be 25 kPa.

Rat Brain Sample. MRE was extended to study brain tissue. A brain was dissected from a laboratory rat and placed in the sample holder on top of agarose gel of 1.0% wt. and surrounded by 0.25% wt gel. The gel of a lower concentration ensured the propagation of the shear waves through the tissues. Figure 17 illustrates the magnitude image, the phase difference map, and the resulting line profile showing the propagation of the shear waves through the sample.

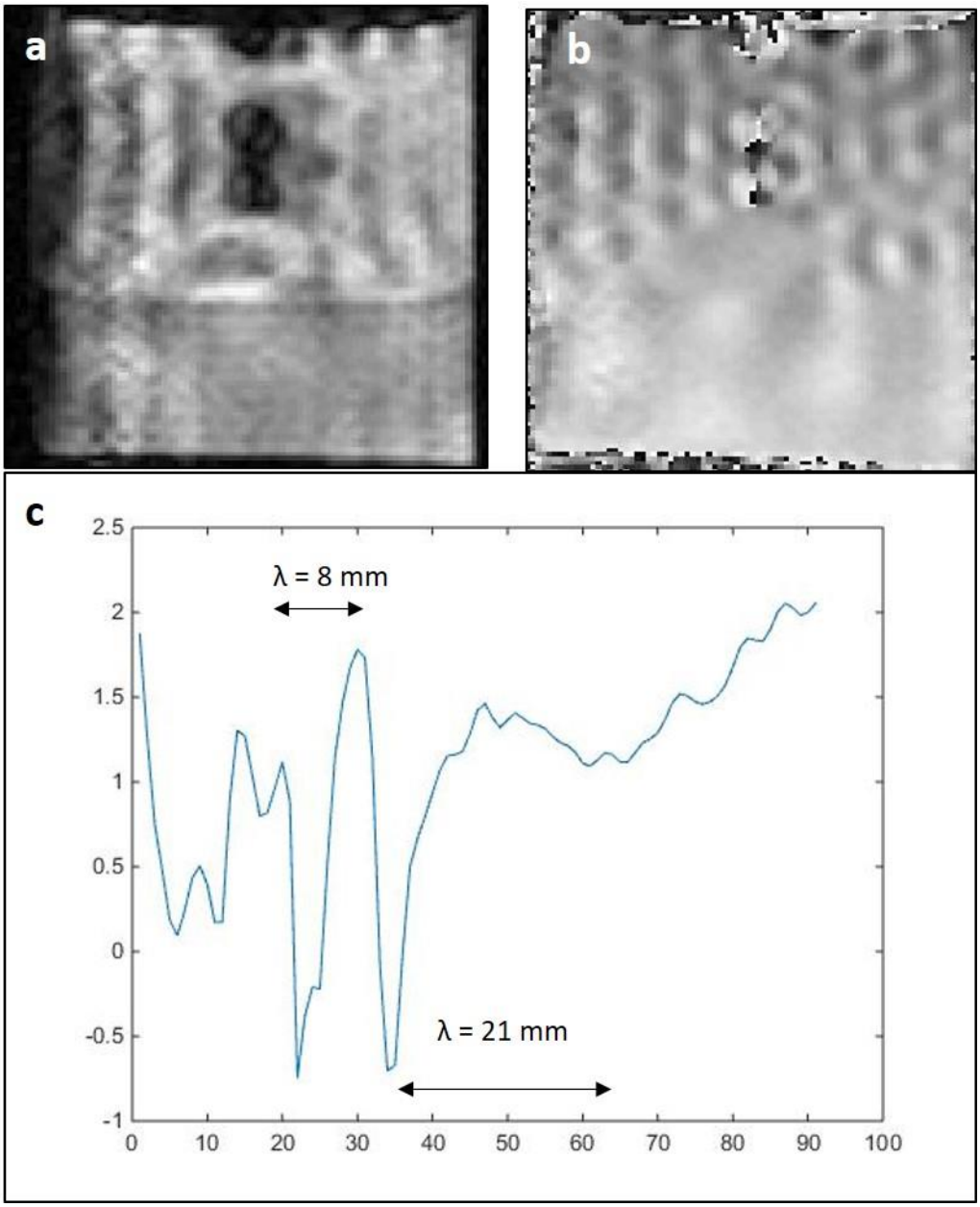

Figure 17: MRE extended to study a rat brain showing the potential to determine mechanical properties. The sample was placed on top of agarose gel of 1.0% wt. concentration and surrounded by agarose gel of 0.25% wt. concentration. a) MR magnitude image of sample with a spin echo based MRE sequence with an in-plane resolution of 0.703 mm, slice thickness of 10 mm, TR of 4 s, TE of 30 ms, NEX of 2, 8 MSG at a frequency 400 Hz. b) Phase difference image showing shear waves. c) A line profile showing change in wavelength as the wave passes through the brain sample.

Discussion

MRI

The MRI results show the capability of the low field system in producing high resolution MR acquisition. MRI is a non-invasive modality that can produce high resolution images of the internal structures within the body. Typical systems used in the clinical setting have high fields ranging from 1.5 – 3 T. These systems are expensive, require constant maintenance, and need special storage. However, the low field system is relatively inexpensive, does not need constant maintenance (i.e. replacement of cooling fluid), and does not need special storage. This makes it powerful in studying various tissues within the lab. Figure 12 shows two images that were acquired with two different samples, a mushroom and a kiwi. Both samples are water abundant and therefore provide strong detectable MR signals. Figure 12a shows the capability of the low field system to produce images that show the physical structure of the sample, whereas Figure 12b shows the capability to image the internal structure of samples non-invasively by capturing a slice at any location in the sample which gives the structural information at that location. Multiple images can be taken, each at a different slice, and can be used to create a 3D animation showing the entire internal structure of the sample.

High field MRI is known for their ability to acquire high resolution images. However, high resolution images can also be obtained at a low magnetic field. This is accomplished by increasing the number of acquisitions. The SNR is proportional to the square root of

the number of acquisitions and therefore a high number of averages results in higher SNR and a better image. Figure 13 shows two images of a rat brain ex vivo with different number of acquisitions. Figure 13a is obtained with 16 averages and Figure 13b is obtained with 256 averages. In the first image, the anatomy of the rat brain is indistinguishable whereas in the second image, with the higher a resolution, the anatomy is clearly visible.

Two main image contrast mechanisms are explained in the section Relaxation Times. Contrast is obtained in images by varying the echo time (TE) and the repetition time (TR). Figure 14 shows contrast obtained in a rat brain by controlling the transverse magnetization (T_2) effects. Biological specimens fixed in preservatives like formalin are difficult to image due to the signal given by the preservative. This decreases the contrast in the sample taken with lower echo times. In Figure 14a, the brain is hardly visible because the contrast between the fixed brain tissue and the formalin is minimal. Since formalin has a shorter T_2 relaxation time than the brain tissue, increasing the TE from 45 ms to 80 ms, creates contrast between the formalin and the brain tissue as shown in Figure 14b. This experiment demonstrated the capability of the low field system in acquiring images with longer echo times, an advantage over high field systems.

MRE

Agarose gel phantoms with high water content produce good MR signals. Furthermore, the concentration of the agarose gel can easily be modified to create samples with different mechanical properties, the values of which are documented in the literature. These properties can be tailored to mimic tissues within the body. Due to these

advantages, agarose gel phantoms are perfect for testing MRE pulse sequences and the inversion algorithm.

The first experiment was conducted with a gel phantom of 0.5% wt. stiffness. As shown in Figure 15, shear waves were transferred in the gel phantom. This validated the developed MRE. The wavelength for the experiment was found to be 7 mm. From the wavelength, the speed at which the waves traveled through the gel phantom can be calculated. At excitation frequency of 300 Hz, the wave speed was calculated to be approximately 2.1 m/s, similar to the published literature (Othman, Xu, Royston, & Magin, 2005).

In the second experiment, MRE was conducted on gel phantom made of two stiffnesses to assess the techniques ability to differentiate between the two gel concentrations. Theoretically, waves traveling through softer materials have a shorter wavelength and waves traveling through stiffer materials have longer wavelengths. In terms of speed, this translates to faster waves in stiffer materials than softer materials. For example, knocking on one side of a table top causes the vibrations on the other side of the table instantly. This is illustrated in Figure 16, where the waves in the softer 0.5% wt. gel (top) have a short wavelength (7 mm) than the waves in the stiffer 1.0% wt. (bottom) gel (14 mm). Thus, the waves are traveling at a faster speed in the stiffer gel; at approximately 5.6 m/s as opposed to 2.8 m/s for the soft gel. This is further confirmed by Figure 16c, a stiffness map produced through the inversion algorithm. The gel on the bottom has a longer wavelength which means that it is stiffer, demonstrated by the stiffness map.

For its application, the low field MRE was extended to study the rat brain as a feasibility study. The brain was fixed sample, so the stiffness measurements were taken. MRE for the study of brain has been conducted at high fields (Boulet et al., 2011), this study illustrated the capability of low field MRE to determine the mechanical properties of the brain as shown in Figure 17. The phase difference map shows the propagation of shear waves through the sample and the line profile shows a change in wavelength as the waves travel from the agar gel to the brain sample. In the study, the mechanical properties were not acquired since the change in the physiology of the tissue due to formalin compromises the stiffness properties. For this reason, the phase difference map shows the brain sample as having similar stiffness as the 1.0% wt. gel. However, the study does demonstrate the feasibility of the low field MRE in studying the brain and can be extended to studying additional tissue types.

Future Application: Study of Tissue Engineered Constructs

Motivation

There is a necessity for replacing bone tissue that has been lost due to trauma. This trauma can be due to physical factors like fractures or due to diseases like osteoporosis and cancer. On average, there are an estimated 10 million cases of fracture related injuries in the US every year (Amini, AR, et.al, 2012). When the fracture is small, or the bone loss is minimal, the human body can naturally replace the bone. Natural bone regeneration is the preferred method of bone healing but for fractures in which a large amount of bone is lost, natural bone healing is unable to replace the bone tissue. Therefore, other methods must be employed to treat these cases of bone loss.

Conventional methods for treatment of bone injuries is through bone grafts. On average, 500,000 graft operations are performed annually in the US, which results in approximately 1.5 billion dollars in bone grafts and bone graft substitute sales. In bone grafting, bone tissue is obtained from either the individual or from cadavers and is implanted at the site of the bone injury (Fillingham & Jacobs, 2016). This gives the bone a framework to use to form a union and heal. Grafts that are obtained from the patient contain live bone tissues that elicit no immune response (since they are from the patient) and readily recruit body cells to repair the bone. However, harvesting bone from the patients require additional surgeries which can cause complications and longer rehabilitation times leading to increased suffering and cost. Bone grafts that are obtained

from donors run the risk of eliciting an immune response that can cause serious injury to the patient. If the body rejects the graft, then it will actively fight the new tissue, which in extreme cases can lead to comma or death. Bone grafts obtained from cadavers offer a matrix for the patient's bone tissue to use as a physical support structure for growth but there are no living cells present in the graft since it is obtained post-mortem. The lack of living cells allow for biocompatibility but lead to a longer healing process since new cells need to be produced and spread along the graft (Spin-Neto et al., 2014).

A potential alternative to transplantation of tissues is offered by tissue engineering (TE). Tissue engineering aims to create biological substitutes for natural tissue within the human body. To accomplish this, it is necessary to use the principles of cell transplantation, biology, materials science, and engineering to combine the essential cells, growth factors, and biomaterials to create functional tissues. Cells that are typically used in tissue engineering are embryonic stem cells or adult stem cells, both of which have the capability to differentiate into cells of different lineages (Caplan, 1994; Langer & Vacanti, 1993). The cells can be made to expand *in vitro* and then seeded onto a scaffold before inducing differentiation either by bioactive signals such as chemical factors or physical excitation (surface-induced, mechanical, or electrical) (Alhadlaq & Mao, 2004; Altman et al., 2002; Heng, Cao, Stanton, Robson, & Olsen, 2004; McBeath, Pirone, Nelson, Bhadriraju, & Chen, 2004). The scaffold provides the stem cells with physical support (matrix) and an environment in which the proper regulation of cell behavior (adhesion, proliferation, migration, and differentiation) can occur.

Mesenchymal stem cells (MSCs) obtained from bone marrow have a strong capability to differentiate into multiple cell lineages such as bone, fat, and cartilage. Bone

marrow is responsible for the formation of osteoblasts and osteocytes. Osteoblasts are responsible for the formation and regulation of bone extracellular matrix deposition and mineralization and osteocytes help with calcification of the bone extracellular matrix. The ability of MSCs to differentiate into osteoblast-like cells makes them ideal for use in bone tissue engineering (Petite et al., 2000; Wang et al., 2018; Pchelintseva & Djamgoz, 2018).

It is essential to characterize any material that is used in design to ensure its proper application and functionality. In TE, understanding of material properties like the stiffness, elasticity, and strength is critical since these properties will influence the success of the construct *in vivo*. Furthermore, these properties change as the tissue develops (initiation of cellular response and remodeling, stem cell differentiation, degradation of scaffold material) (Dado & Levenberg, 2009). Since the tissues are engineered for potential *in vivo* use, they need to be able to provide support for the surrounding tissue. For example, in bone tissue engineering, the scaffold needs to not only provides support for the cells but also needs to provide mechanical support for the injury site. Growth of engineered tissue is typically assessed through microscopy, biochemical assays, or histologic staining. Although these methods provide information about the molecular content of the cell (e.g. staining for alkaline phosphatase (ALSP) provides an early osteogenic marker), they are destructive to the tissue and require the sample be sacrificed. A major challenge in tissue engineering is being able to characterize tissue mechanical properties without harming the living cells in the tissue. This challenge can be addressed through MRE.

Feasibility of MRI and MRE to Characterize TE Bone

MRI has been used to study tissue engineered constructs at a high field strength of 11.74 T (H. Xu, Othman, Hong, Peptan, & Magin, 2006). MRI can assess the growth of tissue engineered bone through quantitative and qualitative measurements. Qualitatively, the growth of the bone has been shown to correlate with a lower imaging intensity caused by the calcification and subsequent elimination of protons from the tissue. Therefore, as the tissue engineered bone grows and becomes stiffer, the signal-to-noise ratio (SNR) in MR images decreases, and the image quality declines. Quantitatively, the T_1 and T2 relaxation times have shown to be dependent on osteogenesis; where a decrease in the parameters showed increased osteogenesis. In their study, Xu, et al., 2006 found that over a four-week period, the T_2 relaxation time for TE bone decreased by 64%. This significant decrease was due to mineral deposition in the extracellular matrix of the osteogenic construct which resulted in regions of solid bone that introduced magnetic susceptibilities, reducing the T_2 relaxation times (H. Xu et al., 2006). This study showed the feasibility of measuring osteogenesis through MR parameters at high field strengths.

MRE has also been used to study TE constructs at high a field strength (Khalilzad-Sharghi et al., 2016; Othman et al., 2012; H. Xu et al., 2006). The development of TE bone is characterized by an increase in the stiffness due to calcification and mineral deposition. Xu, et al., 2006 found that for TE bone, the shear stiffness increased from 11.8 ± 0.4 kPa at week 1 to 15.8 ± 0.5 kPa at week 2. These results were correlated with histologic measurements and provided evidence of osteogenesis in TE bone.

MRI and MRE monitoring of TE bone has been conducted at high field strengths; in the present study, the potential application of low field 0.5 T MRI and MRE is considered.

Methods

Cell Culture. Human mesenchymal stem cells (*h*MSCs) obtained from adult bone marrow (PT-2501, Lonza, Walkersville, MD) were purchased. The *h*MSCs were expanded in Dulbecco's Modified Eagle Medium (12491015, Thermofisher, Waltham, MA) supplemented with 10% fetal bovine serum (10437010, Thermofisher, Waltham, MA) and 1% antibiotic mixture containing penicillin, streptomycin, amphotericin B (152400672, Thermofisher). The cells were incubated at 37 °C with 5.0% CO_2 and expanded to the population essential for the study.

Scaffold Preparation. Fabricated protein silk scaffolds were obtained from Dr. David Kaplan's lab from Tuffts University. The scaffolds were 12 mm in diameter and 6-8 mm in height with a pore size of 500-600 micrometers. Prior to seeding, the scaffolds were autoclaved in distilled water at 121°C and 14-16 psi for 20 minutes in the liquid cycle for sterilization. The sterile scaffolds were placed in the incubator in culture media for 2 hours before seeding. A standard 24-well plate was used.

Scaffold Seeding. The *h*MSCs were seeded onto the scaffold at a density of 2.0 x 10^6 cells per scaffold in a cell suspension of 200 µl. To ensure proper spread of the cells, the cell suspension was dispensed in a dropwise fashion over the entire surface of the scaffold. After seeding, the scaffold was placed in the incubator for 15 minutes. After 15 minutes, the scaffold was flipped 180° and 20 µl of cell culture media was added to

maintain hydration. This process was repeated for a total of four times, after which the scaffold was aspirated to remove the growth media. Each scaffold was placed in 2 ml of osteogenic differentiation media (SCM121, MilliporeSigma,St. Louism MO), which was exchanged every two-three days. A total of 5 scaffolds were used for the study.

Scaffold Imaging Procedure. Three scaffolds were imaged with MRI, two scaffolds were imaged with MRE, and three scaffolds were set aside for proteomics. The scaffolds were removed from the incubator and immediately placed in a specialized holder for MR imaging. MR imaging of the scaffolds was conducted at week 0, week 2, and week 4. Imaging was conducted with a spin echo imaging sequence with a TR of 2 s, a TE of 60 ms, in-plane resolution of 0.195 mm, and NEX of 256. For MRE, the scaffold was immersed in agarose gel of 0.25% wt. concentration and placed in a MRE holder. Imaging was conducted with a spin echo based MRE sequence with a TR of 4 s, a TE of 30 ms, an in-plane resolution of 0.273 mm, NEX of 16, and 4 MSG. MRE was conducted at week 0 and week 2. Imaging procedure of scaffolds is summarized in Table 3.

Table 3: Breakdown for the imaging of tissue engineered constructs. A total of 8 scaffolds were imaged (3 through MRI, 2 through MRE, 3 through Proteomics).

Imaging Type	Week 0	Week 2	Week 4
MRI	X	X	X
MRE	X	X	
Proteomics	X	X	X

Preliminary Results of Tissue Engineered Bone

MRI. As shown in Figure 18, low field MRI can image the engineered construct with high resolution. It is expected that as the constructs undergo osteogenesis, there will be a decrease in the MR signal intensity which will result in a decrease in the image SNR.

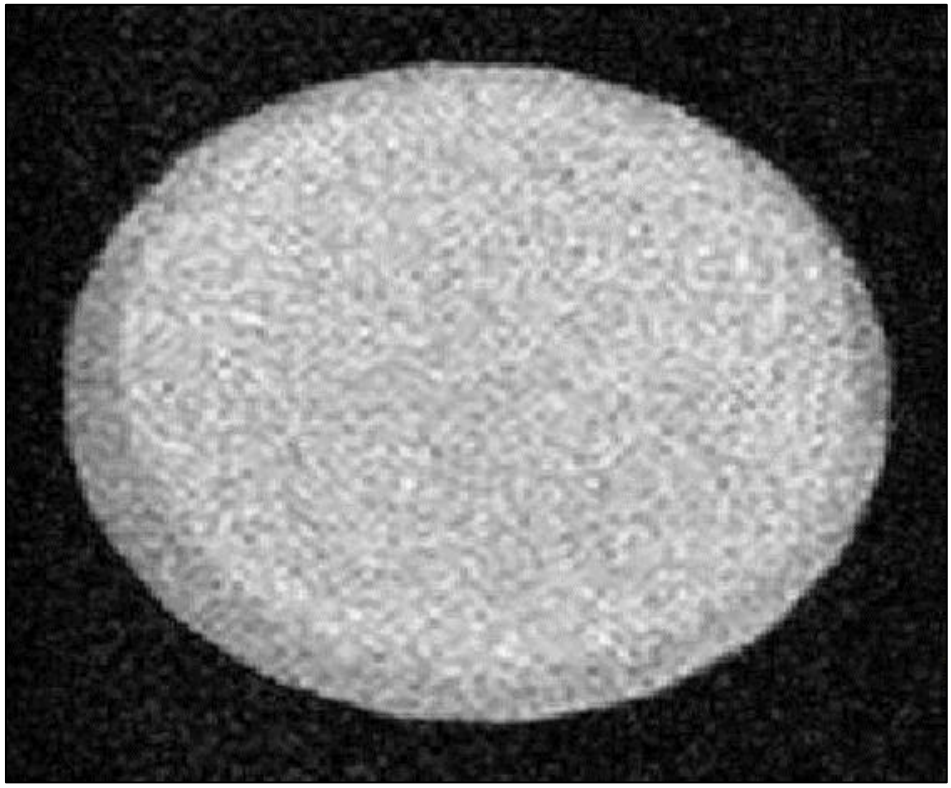

Figure 18: MR image of a tissue engineered bone at week 0 showing the capability of the low field system in acquiring high resolution images. The image was acquired with a spin echo sequence with an in-plane resolution of 0.195 mm, a TR of 2 s, TE of 60 ms, slice thickness of 8 mm, and 128 NEX.

MRE. Figure 19 shows a stiffness map of the TE bone construct at week 0. From the map, the stiffness of the TE bone is approximated at 5 kPa at week 0. It is expected that as the osteogenesis occurs, the stiffness should increase which will be indicated by the stiffness map.

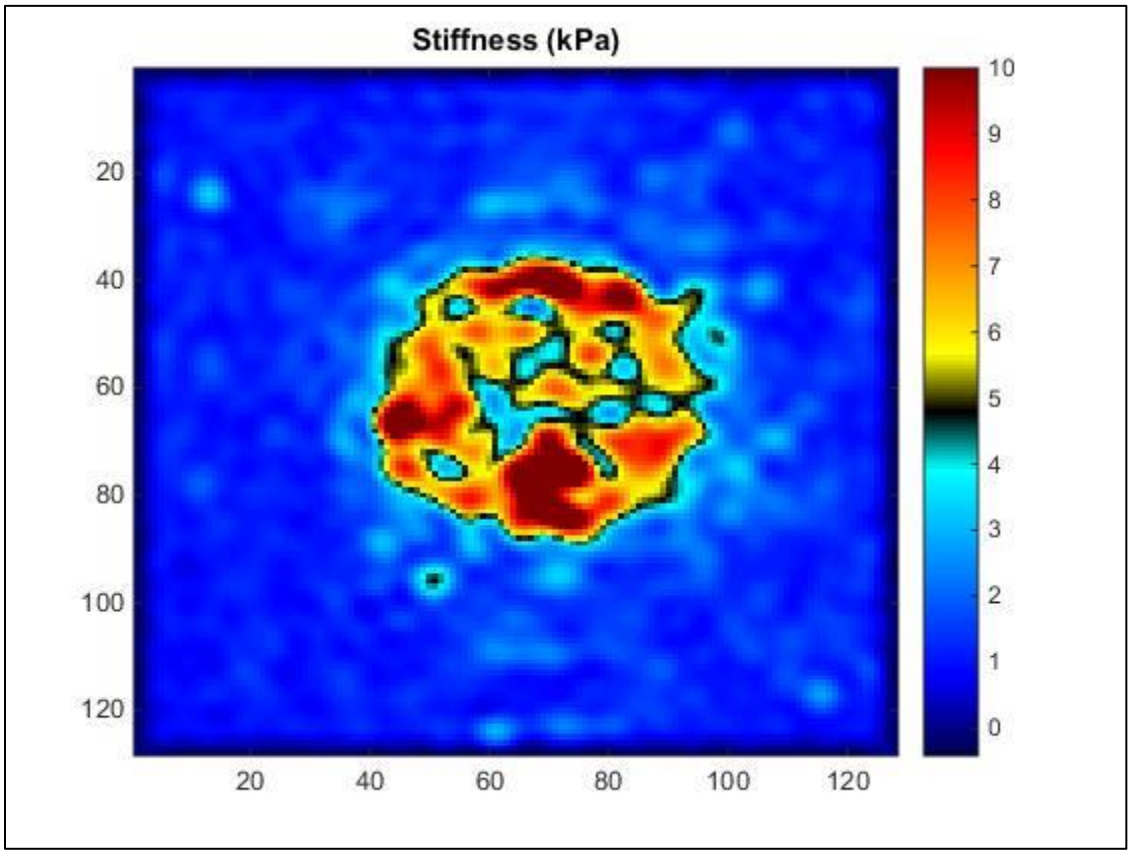

Figure 19: Stiffness map for TE bone at week 0 obtained through a spin echo based MRE sequence. The sample was placed in 0.25% wt. agarose gel. The map was produced with an in-plane resolution of 0.273 mm, a TR of 4 s, TE of 30 ms, slice thickness of 8 mm, MSG frequency of 400 Hz, 4 MSG waves, and 16 NEX.

Summary

The ability of the low field MR system in providing high resolution images can significantly change many fields of study. This study demonstrated that a 0.5 T low field MRI can be utilized to image various types of samples and samples of different sizes and do so with excellent contrast. The study explored the capability of the low field MR system to obtain contrast between tissues and found that relaxation parameters like spin-spin relaxation (T_2) can be manipulated to influence the contrast. Furthermore, in this study, the low field MR system was modified into one capable of performing MR elastography, a technique used to accurately and noninvasively determine the mechanical properties of soft samples. The sensitivity of MRE was explored through the study of a rat brain and it was determined that MRE can successfully provide estimates of the mechanical properties of the brain. This also demonstrated that low field MRE can be extended to studying the stiffness parameters of other tissues.

An additional and significant application of low field MRI and MRE is for the study of tissue engineered bone. Low field MR systems have the advantage of being able to image stiffer materials and so they are ideal in assessing the growth of the bone. As the bone grows and increases in stiffness, the growth can be assessed through imaging and measurement of MR parameters like the T_2 relaxation. Additionally, low field MRE can also provide quantitative measures of mechanical properties which can be correlated with the MR images and parameters to provide solid evidence of bone growth.

Low field MRI is a powerful tool that has many applications. However, there are several limitations that need to be considered before its use in experimental studies. It was demonstrated that low field systems can produce MR images with resolution comparable to high field systems. These images are obtained by increasing the number of acquisitions, which results in an increase in the scan time. Therefore, the desired resolution needs to be balanced with the desired scan time. This becomes crucial in imaging engineered tissue where extended scan times can result in the death of the cells. Furthermore, MRE is highly dependent on the characterization of the actuator resonance frequency. If the proper frequency is not used, it can result in inadequate displacement which could compromise mechanical property measurements. This can cause a misinterpretation of the results. However, this issue can be avoided by determining the resonance frequency of the actuator for each experimental study. Overall, the benchtop low field MRI is a transformative tool that has wide applications. For example, it is expected that the successful measure of osteogenesis through low field MR imaging and MRE will transform the field of tissue engineering; it represents a low-cost tool that accurately provides information about tissue growth.

References

Alhadlaq, A., & Mao, J. J. (2004). Mesenchymal stem cells: isolation and therapeutics. *Stem Cells and Development*, *13*(4), 436–448. https://doi.org/10.1089/scd.2004.13.436

Altman, G. H., Horan, R. L., Martin, I., Farhadi, J., Stark, P. R. H., Volloch, V., … Kaplan, D. L. (2002). Cell differentiation by mechanical stress. *FASEB Journal: Official Publication of the Federation of American Societies for Experimental Biology*, *16*(2), 270–272. https://doi.org/10.1096/fj.01-0656fje

Balter, S. (1987). An introduction to the physics of magnetic resonance imaging. *Radiographics: A Review Publication of the Radiological Society of North America, Inc*, *7*(2), 371–383. https://doi.org/10.1148/radiographics.7.2.3448640

Batheja, M., Vargas, H., Silva, A. M., Walker, F., Chang, Y.-H., De Petris, G., & Silva, A. C. (2015). Magnetic resonance elastography (MRE) in assessing hepatic fibrosis: performance in a cohort of patients with histological data. *Abdominal Imaging*, *40*(4), 760–765. https://doi.org/10.1007/s00261-014-0321-8

Besa, C., Wagner, M., Lo, G., Gordic, S., Chatterji, M., Kennedy, P., … Taouli, B. (2017). Detection of liver fibrosis using qualitative and quantitative MR elastography compared to liver surface nodularity measurement, gadoxetic acid uptake, and serum markers. *Journal of Magnetic Resonance Imaging*, n/a-n/a. https://doi.org/10.1002/jmri.25911

Boulet, T., Kelso, M. L., & Othman, S. F. (2011). Microscopic magnetic resonance elastography of traumatic brain injury model. *Journal of Neuroscience Methods*, *201*(2), 296–306. https://doi.org/10.1016/j.jneumeth.2011.08.019

Brown, R. W., Haacke, E. M., Cheng, Y.-C. N., Thompson, M. R., & Venkatesan, R. (2014). *Magnetic Resonance Imaging: Physical Principles and Sequence Design*. John Wiley & Sons.

Caplan, A. I. (1994). The mesengenic process. *Clinics in Plastic Surgery*, *21*(3), 429–435.

Dado, D., & Levenberg, S. (2009). Cell-scaffold mechanical interplay within engineered tissue. *Seminars in Cell & Developmental Biology*, *20*(6), 656–664. https://doi.org/10.1016/j.semcdb.2009.02.001

Doyley, M. M., & Parker, K. J. (2014). Elastography: general principles and clincial applications. *Ultrasound Clinics*, *9*(1), 1–11. https://doi.org/10.1016/j.cult.2013.09.006

Faria, S. C., Ganesan, K., Mwangi, I., Shiehmorteza, M., Viamonte, B., Mazhar, S., … Sirlin, C. B. (2009). MR Imaging of Liver Fibrosis: Current State of the Art. *RadioGraphics*, *29*(6), 1615–1635. https://doi.org/10.1148/rg.296095512

Faruk, T., Islam, M. K., Arefin, S., & Haq, M. Z. (2015). The Journey of Elastography: Background, Current Status, and Future Possibilities in Breast Cancer Diagnosis. *Clinical Breast Cancer*, *15*(5), 313–324. https://doi.org/10.1016/j.clbc.2015.01.002

Fillingham, Y., & Jacobs, J. (2016). Bone grafts and their substitutes. *Bone Joint J*, *98-B*(1 Supple A), 6–9. https://doi.org/10.1302/0301-620X.98B.36350

Hawley, J. R., Kalra, P., Mo, X., Raterman, B., Yee, L. D., & Kolipaka, A. (2017). Quantification of breast stiffness using MR elastography at 3 Tesla with a soft sternal driver: A reproducibility study. *Journal of Magnetic Resonance Imaging*, *45*(5), 1379–1384. https://doi.org/10.1002/jmri.25511

Heng, B. C., Cao, T., Stanton, L. W., Robson, P., & Olsen, B. (2004). Strategies for Directing the Differentiation of Stem Cells Into the Osteogenic Lineage In Vitro. *Journal of Bone and Mineral Research*, *19*(9), 1379–1394. https://doi.org/10.1359/JBMR.040714

Jéquier, E., & Constant, F. (2010). Water as an essential nutrient: the physiological basis of hydration. *European Journal of Clinical Nutrition*, *64*(2), 115–123. https://doi.org/10.1038/ejcn.2009.111

Khalilzad-Sharghi, V., Han, Z., Xu, H., & Othman, S. F. (2016). MR elastography for evaluating regeneration of tissue-engineered cartilage in an ectopic mouse model. *Magnetic Resonance in Medicine*, *75*(3), 1209–1217. https://doi.org/10.1002/mrm.25745

Kruse, S. A., Rose, G. H., Glaser, K. J., Manduca, A., Felmlee, J. P., Jack, C. R., & Ehman, R. L. (2008). Magnetic resonance elastography of the brain. *NeuroImage*, *39*(1), 231–237. https://doi.org/10.1016/j.neuroimage.2007.08.030

Langer, R., & Vacanti, J. P. (1993). Tissue engineering. *Science (New York, N.Y.)*, *260*(5110), 920–926.

Lipp, A., Skowronek, C., Fehlner, A., Streitberger, K.-J., Braun, J., & Sack, I. (2018). Progressive supranuclear palsy and idiopathic Parkinson's disease are associated with local reduction of in vivo brain viscoelasticity. *European Radiology*, 1–8. https://doi.org/10.1007/s00330-017-5269-y

Mariappan, Y. K., Glaser, K. J., & Ehman, R. L. (2010). Magnetic resonance elastography: A review. *Clinical Anatomy*, *23*(5), 497–511. https://doi.org/10.1002/ca.21006

McBeath, R., Pirone, D. M., Nelson, C. M., Bhadriraju, K., & Chen, C. S. (2004). Cell shape, cytoskeletal tension, and RhoA regulate stem cell lineage commitment. *Developmental Cell*, *6*(4), 483–495.

MRI at a Glance, 2nd ed. (2012). *Radiology*, *263*(2), 362–362. https://doi.org/10.1148/radiol.12124005

Murphy, M. C., Jones, D. T., Jack, C. R., Glaser, K. J., Senjem, M. L., Manduca, A., … Huston, J. (2016). Regional brain stiffness changes across the Alzheimer's disease spectrum. *NeuroImage. Clinical*, *10*, 283–290. https://doi.org/10.1016/j.nicl.2015.12.007

Muthupillai, R., Lomas, D. J., Rossman, P. J., Greenleaf, J. F., Manduca, A., & Ehman, R. L. (1995). Magnetic Resonance Elastography by Direct Visualization of Propagating Acoustic Strain Waves. *Science*, *269*(5232), 1854–1857.

Muthupillai, Raja, & Ehman, R. L. (1996). Magnetic resonance elastography. *Nature Medicine*, *2*(5), nm0596-601–601. https://doi.org/10.1038/nm0596-601

Othman, S. F., Curtis, E. T., Plautz, S. A., Pannier, A. K., Butler, S. D., & Xu, H. (2012). MR elastography monitoring of tissue-engineered constructs. *NMR in Biomedicine*, *25*(3), 452–463. https://doi.org/10.1002/nbm.1663

Othman, S. F., Xu, H., Royston, T. J., & Magin, R. L. (2005). Microscopic magnetic resonance elastography (μMRE). *Magnetic Resonance in Medicine*, *54*(3), 605–615. https://doi.org/10.1002/mrm.20584

Pchelintseva, E., & Djamgoz, M. B. A. (2018). Mesenchymal stem cell differentiation: Control by calcium-activated potassium channels. *Journal of Cellular Physiology*, *233*(5), 3755–3768. https://doi.org/10.1002/jcp.26120

Petite, H., Viateau, V., Bensaid, W., Meunier, A., de Pollak, C., Bourguignon, M., … Guillemin, G. (2000). Tissue-engineered bone regeneration. *Nature Biotechnology*, *18*(9), 959–963. https://doi.org/10.1038/79449

Prince, J. L., & Links, J. M. (2006). *Medical imaging signals and systems*. Pearson Prentice Hall Upper Saddle River.

Rouvière, O., Yin, M., Dresner, M. A., Rossman, P. J., Burgart, L. J., Fidler, J. L., & Ehman, R. L. (2006). MR Elastography of the Liver: Preliminary Results. *Radiology*, *240*(2), 440–448. https://doi.org/10.1148/radiol.2402050606

Shah, N. S., Kruse, S. A., Lager, D. J., Farell-Baril, G., Lieske, J. C., King, B. F., & Ehman, R. L. (2004). Evaluation of renal parenchymal disease in a rat model with

magnetic resonance elastography. *Magnetic Resonance in Medicine*, *52*(1), 56–64. https://doi.org/10.1002/mrm.20101

Spin-Neto, R., Stavropoulos, A., Coletti, F. L., Faeda, R. S., Pereira, L. A. V. D., & Marcantonio, E. (2014). Graft incorporation and implant osseointegration following the use of autologous and fresh-frozen allogeneic block bone grafts for lateral ridge augmentation. *Clinical Oral Implants Research*, *25*(2), 226–233. https://doi.org/10.1111/clr.12107

Wang, R., Liu, W., Du, M., Yang, C., Li, X., & Yang, P. (2018). The differential effect of basic fibroblast growth factor and stromal cell-derived factor-1 pretreatment on bone morrow mesenchymal stem cells osteogenic differentiation potency. *Molecular Medicine Reports*, *17*(3), 3715–3721. https://doi.org/10.3892/mmr.2017.8316

Xu, H., Othman, S. F., Hong, L., Peptan, I. A., & Magin, R. L. (2006). Magnetic resonance microscopy for monitoring osteogenesis in tissue-engineered construct in vitro. *Physics in Medicine and Biology*, *51*(3), 719–732. https://doi.org/10.1088/0031-9155/51/3/016

Xu, L., Lin, Y., Xi, Z. N., Shen, H., & Gao, P. Y. (2007). Magnetic Resonance Elastography of the Human Brain: A Preliminary Study. *Acta Radiologica*, *48*(1), 112–115. https://doi.org/10.1080/02841850601026401

Yin, M., Talwalkar, J. A., Glaser, K. J., Manduca, A., Grimm, R. C., Rossman, P. J., … Ehman, R. L. (2007). Assessment of Hepatic Fibrosis With Magnetic Resonance Elastography. *Clinical Gastroenterology and Hepatology*, *5*(10), 1207-1213.e2. https://doi.org/10.1016/j.cgh.2007.06.012